

Experimental investigation of electromagnetic fields from Helmholtz type circular coils
by Michael William Sampsel

A thesis submitted in partial fulfillment of the requirements for the degree of MASTER OF SCIENCE in Electrical Engineering
Montana State University
© Copyright by Michael William Sampsel (1982)

Abstract:
The subject of this thesis is to measure spatial variations of electromagnetic fields from circular time varying current sources. In order to verify experimental measurements digital computer models of the fields in free space were derived. Fields within Ringer's solution contained within cylindrical and rectangular boundaries were measured experimentally. It was found that neither boundary provides for uniform field magnitudes throughout the containers regardless of the direction of the applied magnetic field from the circular current loops. A coaxial cylindrical container was suggested as a means of providing more uniform fields throughout the solution.

A brief Fourier analysis of several types of waveforms induced in the Ringer's solution was also performed.

STATEMENT OF PERMISSION TO COPY

In presenting this thesis in partial fulfillment of the requirements for an advanced degree at Montana State University, I agree that the Library shall make it freely available for inspection. I further agree that permission for extensive copying of this thesis for scholarly purposes may be granted by my major professor, or, in his absence, by the Director of Libraries. It is understood that any copying or publication of this thesis for financial gain shall not be allowed without my written permission.

Signature Michael W. Sampsel

Date May 10, 1982

EXPERIMENTAL INVESTIGATION OF ELECTROMAGNETIC FIELDS FROM HELMHOLTZ TYPE CIRCULAR COILS

by

MICHAEL WILLIAM SAMPSEL

A thesis submitted in partial fulfillment
of the requirements for the degree

of

MASTER OF SCIENCE

in

Electrical Engineering

Approved:

Bruce R. McLeod
Chairman, Examining Committee

D. A. Pierre
Head, Major Department

Michael Malone
Graduate Dean

MONTANA STATE UNIVERSITY
Bozeman, Montana

June, 1982

ACKNOWLEDGMENTS

The author extends appreciation and thanks to Dr. A. A. Pilla and Electro-Biology Inc. for the use of the BI-OSTEOGEM. The author would also like to thank Dr. Daniel March and Dr. Donald Pierre for their suggestions in the preparation of this paper. The author is especially grateful for Dr. Bruce R. McLeod's support, suggestions and encouragement throughout the project. Most of all the author is thankful for the support given from his wife and his parents.

TABLE OF CONTENTS

	Page
VITA	ii
ACKNOWLEDGMENTS	iii
TABLE OF CONTENTS	iv
LIST OF TABLES	vi
LIST OF FIGURES	vii
ABSTRACT	x
INTRODUCTION	1
Chapter	
I SPATIAL VARIATIONS OF ELECTRIC AND MAGNETIC FIELDS IN FREE SPACE	3
Theoretical Fields for Circular Current Loops	3
Selection Inductive Test Systems	5
Experimental Methods and Procedures	8
Theoretical and Experimental Results	12
Accuracy of Results	17
II FOURIER ANALYSIS	18
Current Density a Result of Fourier Analysis	21
III BOUNDARY CONDITION CONSIDERATIONS AN EXPERIMENTAL VIEW	30
Experimental Procedure	30
Experimental Results	36
Horizontal Orientation	36
Vertical Orientation	40
IV CONCLUSIONS	46
Suggested Optimum System	48
BIBLIOGRAPHY	50

Page

APPENDICES 53
APPENDIX A—Fields Program 54
APPENDIX B—Fourier Program 57
APPENDIX C—Time Program 59
APPENDIX D—Mutual Inductance, Coefficient of Coupling Current and Current Derivative Determinations 61
APPENDIX E—V(t) for Different ITS's and I(t) Figures 64
APPENDIX F—Method to Calculate B_z from Experimental Measurements 66
APPENDIX G—Time Output 68
APPENDIX H—Factors Used to Find the Voltage Spectrum of Figure 13 70
APPENDIX I—Proof of Equal Energy and Equal Area of the Square Wave Approximation 73
APPENDIX J—"Student's t" Test 76
APPENDIX K—RMS Error Evaluation 79
APPENDIX L—Definitions of Variables and Operations 82

LIST OF TABLES

Table		Page
1.	Values of $\partial I(t)/\partial t$ for Different ITS's	9
2.	Main Components for Various Repetition Rates	20
3.	Relative Changes in E_x for x,y Positions, Horizontal Orientation	37
4.	Relative E_x Values Corresponding to Figure 32 Coils Vertical z Position as Figure 33	44
5.	Relative E_x Values Corresponding to 0.5 in. Water, Coils Vertical	44
Appendix Tables		
6.	Measured Values of E_x and E_y and Corresponding t Values	78
7.	Values Used in Standard Error Estimates	80
8.	RMS Value of Difference and Measured Average Values	81

LIST OF FIGURES

Figure		Page
1.	Coordinate System	5
2.	Driving Coil System (DCS) and Inductive Test System (ITS) Coils	7
3.	DCS	8
4.	Total EMF of ITS	11
5.	Positive Portion EMF of ITS	11
6.	Theoretical Fields, z = 0 Plane	13
7.	Experimental Fields, z = 0 Plane	14
8.	Theoretical Fields, z = 2cm Plane	15
9.	Experimental Fields, z = 2cm Plane	16
10.	Square Wave Approximation of Burst Used in FOURIER	23
11.	Approximation Single Pulse Waveform	24
12.	Enlargement of the Negative Portion of Figure 11	24
13.	Voltage Spectrum of Figure 11	25
14.	Voltage Spectrum 11Hz Burst	26
15.	Voltage Spectrum 15Hz Burst	27
16.	Voltage Spectrum 20Hz Burst	28
17.	LP Outburst (38kHz)	29
18.	LP Output (one megaHz)	29
19.	DCS Horizontal	31
20.	DCS Vertical	31

Figure		Page
21.	Dipole Fields Measured	32
22.	X,Y Positions Coils Horizontal	33
23.	Cylindrical Positions Coils Horizontal	34
24.	Dipole EMF Position 14, z=0	35
25.	Dipole EMF Position 25, z=3.5cm	35
26.	Dipole EMF Position 25, z=2.3cm	35
27.	z Positions Both Containers Coils Normal	37
28.	Field Plot for Positions of Figure 21	38
29.	E_ϕ Plot Cylindrical Boundaries	39
30.	Comparison of E_y and E_z for Horizontal and Vertical Orientations	41
31.	Plane x,y at z = 2.5 in.	42
32.	Positions Coils Vertical	43
33.	Relative z Position and Water Level	43
34.	$\bar{E}$ Lines for Vertical Coils	46
35.	Vertical Coils	47
36.	Horizontal Coils	48
37.	Proposed Optimum Boundary	49
38.	Proposed Optimum for Cells	49
Appendix Figures		
39.	DCS Schematic	62
40.	Circuit to Find M	62

Figure		Page
41.	Circuit to Find M	62
42.	V(t) LITS of 2.0 microHenerys	65
43.	V(t) LITS of 4.0 microHenerys	65
44.	I(t)	65
45.	Time Output 11Hz Burst	69
46.	Waveform Used to Compute Real and Imaginary Parts	72
47.	Voltage and Current Waveforms Equal Energy Calculations	75

ABSTRACT

The subject of this thesis is to measure spatial variations of electromagnetic fields from circular time varying current sources. In order to verify experimental measurements digital computer models of the fields in free space were derived. Fields within Ringer's solution contained within cylindrical and rectangular boundaries were measured experimentally. It was found that neither boundary provides for uniform field magnitudes throughout the containers regardless of the direction of the applied magnetic field from the circular current loops. A coaxial cylindrical container was suggested as a means of providing more uniform fields throughout the solution.

A brief Fourier analysis of several types of waveforms induced in the Ringer's solution was also performed.

INTRODUCTION

Electromagnetic energy has been shown to be a catalyst to certain functions of selected biological systems. These catalytic properties are now being used clinically to heal recalcitrant bone fractures. Several researchers have conducted numerous experiments testing the effects of electromagnetic energy on biological systems [1,2,3]. Some systems Dr. A. A. Pilla has tested include: calcium uptake in embryonic chick tibia [4], modulation of rat radial osteotomy repair (with P. Christel and G. Cerf)[5], and lifespan extension (electromagnetic energy in addition to chemotherapy for positive results, with Dr. Steve Smith) of rats with melanomas [6]. Because Pilla used induced energy as opposed to dc delivered by metal conductors, the possibility of a chemical reaction between the system and the apparatus used to apply energy is eliminated.

Certain experiments of Pilla's have shown that slight changes in waveforms applied to biological systems produce dramatically different results. For example, by changing only the repetition rate of a five msec, burst type waveform, percent change versus controls vary from slightly negative to largely positive [5]. Although some Fourier analysis was done in order to determine an approximate upper frequency limit of the spectral components of the waveform, it did not become clear why different waveforms caused different results.

When cells are exposed to induced energy the question arises: are all cells throughout the system exposed to the same magnitudes of $\bar{E}$, the electric field intensity vector, as well as $\bar{H}$, the magnetic field intensity vector? Obtaining boundary conditions such that all cells of the system are exposed to uniform magnitude $\bar{E}$ and $\bar{H}$ could contribute to the study of biological response versus magnitudes of the induced fields. Further, Gandhi [7] has indi-

cated that the direction of a propagating wave could be significant in regards to biological effects. Thus, perhaps knowledge of direction of the fields with respect to individual cells could be important.

The main contribution of this thesis is to study field patterns in homogeneous material within various boundary conditions. Rectangular and cylindrical containers were considered as boundaries for Ringer's solution and electric field patterns within the containers were determined experimentally for different directions of the applied time varying magnetic field. Although not considered in this thesis theoretical models of electric field intensity within the rectangular containers have been derived by Dr. Bruce R. McLeod [8]. Because biological cells introduce a boundary not considered in any measurements or derivations in this thesis, the values of the fields and currents within the cell were not determined. However, this thesis will show that cells at various positions of the system will certainly be exposed to different magnitudes of external currents and fields and the degree of variation of the exposure depends upon position as well as orientation of the biological system.

Chapter I

SPATIAL VARIATIONS OF ELECTRIC AND MAGNETIC FIELDS IN FREE SPACE

Theoretical Fields for Circular Current Loops

In order to obtain theoretical models for $\bar{E}$ and $\bar{B}$, the electric field intensity and magnetic field density vectors respectively, it is appropriate to begin with Maxwell's second equation

$$\nabla \cdot \bar{B} = 0 \tag{1}$$

From Equation 1 through the use of a vector identity it can be shown that

$$\bar{B} = \nabla \times \bar{A} \tag{2}$$

The direction of the applied field and low back EMF dictate that only the phi (ϕ) component of $\bar{A}$ exists, where phi is the direction shown in Figure 1. From symmetry $\partial/\partial\phi = 0$ so it follows that

$$\nabla \cdot \bar{A} = 0 \tag{3}$$

for cylindrical coordinates. Thus, Equations 2 and 3 totally define the vector $\bar{A}$. From Maxwell's third equation,

$$\nabla \times \bar{E} = - \partial\bar{B}/\partial t \tag{4}$$

with the use of Equation 1 and the vector identity, the curl of the gradient of any scalar is identically zero, Equation 5 results

$$\bar{E} = - \nabla V - \partial\bar{A}/\partial t \tag{5}$$

Since $- \nabla V$ is the solution to the homogeneous form of Equation 4, the solution for $\bar{E}$ with $\partial I(t)/\partial t$ as well as $\partial\bar{B}/\partial t$ equal to zero, must be $- \nabla V$. However, since $\rho = 0$, i.e., no

free charge density between the coils as well as at the source, it follows that $V = 0$. Therefore,

$$\bar{E} = - \partial \bar{A}/\partial t \tag{6}$$

The two equations used to determine spatial variations of field quantities in free space, with a circular current loop the source, have been derived as follows [9,10]:

$$A\phi = \frac{\mu I}{k} \left(\frac{a}{r}\right)^{1/2} [(1 - \tfrac{1}{2} k^2)K - E] \tag{7}$$

$$B_z = \frac{\mu I}{2 [(a + r)^2 + z^2]^{1/2}} \left[K + \left(\frac{a^2 - r^2 - z^2}{(a - r)^2 + z^2}\right)E\right] \tag{8}$$

Where: I and a is the current and fixed radius respectively of the loop; $k^2 = 4ar/[(a + r)^2 + z^2]$; μ is the permeability constant; K and E are elliptic integrals of the first and second kinds respectively, and z and r are the running variables of the coordinate system as shown in Figure 1.

It is noted that both of the references cited for Equations 7 and 8 derived them for constant currents. However, they still hold for I replaced by I(t), a time varying current. Also, an equation for the radial component of the magnetic field density vector B_r was given by the references cited. Since B_r was found to be nearly an order of magnitude smaller than B_z in the region of constant B_z, B_r was ignored.

In order to obtain theoretical free space values of B_z and E_ϕ versus position, Equations 7 and 8 were programmed into a digital computer. Since the system was assumed linear, the principle of superposition was used to calculate relative field variations for a fixed z plane versus r. Once the magnitudes of the field quantities were obtained for two single turn current loops of specific dimensions, scale factors were applied for our case to obtain Figures 6 and 8. The multiplying factors included: the number of turns per coil of the

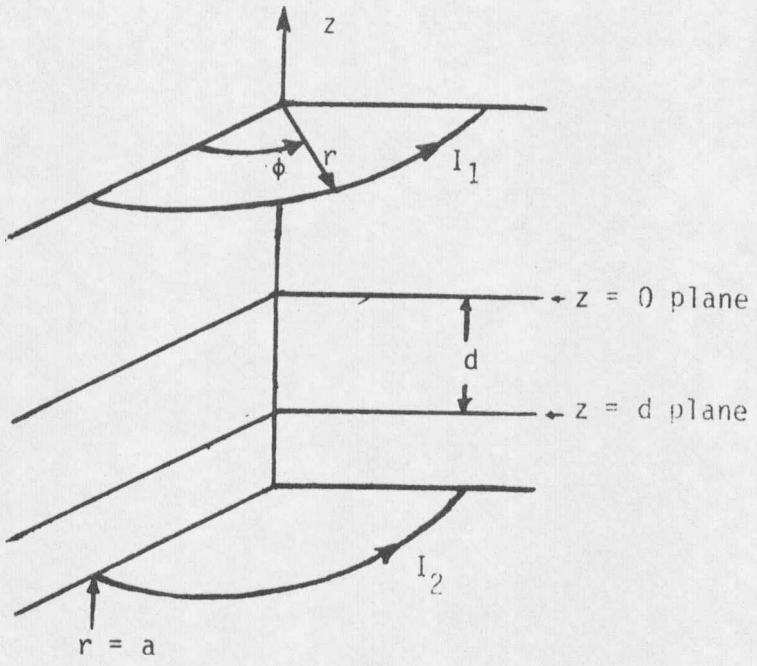


Fig. 1. Coordinate System.

driving coil system (DCS) and the value of the $\partial I(t)/\partial t$ and $I(t)$ at some specific time (t_1) for E_ϕ and B_z respectively. Methods used to determine $I(t)$ and $\partial I(t)/\partial t$ are shown in Appendix D. Also, included in the program (FIELDS) was a subroutine to evaluate elliptic integrals [11]; the program is displayed in Appendix A.

Selection Inductive Test Systems

In order to verify the theoretical equations for E_ϕ and B_z, a method of measurement had to be devised. This section explains the theory used to choose the inductive test systems (ITS's) used to gather data.

The coupling of $\bar{E}$ and $\bar{B}$, as seen in Equation 4, creates the possibility of calculating $\bar{E}$ and $\bar{B}$ as functions of r and z from measurements of the same quantity. From Equation 4 using Stoke's theorem it follows that

$$\oint \bar{E} \cdot \bar{dl} = - \int \frac{\partial \bar{B}}{\partial t} \cdot \bar{ds} = \partial \Phi / \partial t \tag{9}$$

Equation 9 is equal to the induced electromotive force (EMF). However, the different differentials of the two integrals make it convenient to have a separate source of EMF for $\bar{E}$ and $\bar{B}$ determinations. Thus, in order to verify plots obtained theoretically, different sources of EMF were used for $\bar{E}$ and $\bar{B}$.

Although $\bar{E}$ varies with r, z and time it does not vary with ϕ; also, only a ϕ component of $\bar{E}$ exists. Therefore, since

$$\bar{dl} = r \, d\phi \bar{a\phi} \tag{10}$$

and since E_ϕ is a constant of integration in Equation 9 a measured EMF with a proper device allows E_ϕ to be calculated for a particular radius in a constant z plane.

Unfortunately, since B_z varies with respect to r, B_z is not a constant of integration. However, assuming the theoretical plots to be correct (Figures 6 and 8), B_z is nearly constant for the range of r from zero to four centimeters. Therefore, B_z was assumed constant with respect to integration in that range and a suitable differential is

$$\bar{ds} = r' \, dr' \, d\phi' \bar{az} \tag{11}$$

Primed variables indicate that the center of the $\bar{ds}$ did not necessarily coincide with the center of the coordinate system of the DCS as shown in Figure 2.

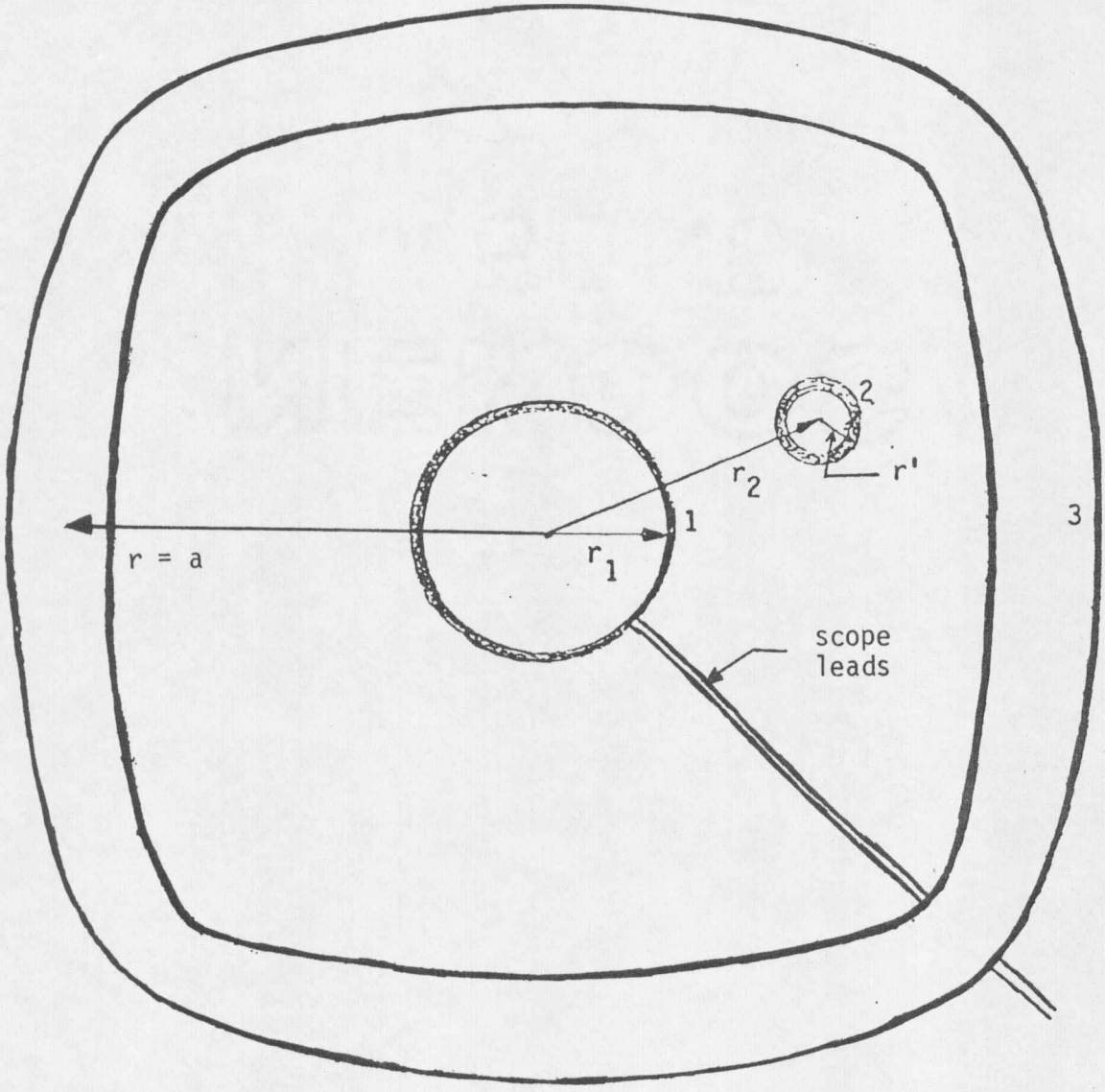


Fig. 2. Driving Coil System (DCS) and Inductive Test System (ITS) Coils. (1) ITS to measure E_ϕ at $r = r_1$. (2) ITS of radius r' to measure B_z at r_2. (3) Geometry of a coil of (DCS) actual size.

Experimental Methods and Procedures

The equipment used to create the fields for experimental measurements is illustrated in Figure 3. The DCS was supplied by Dr. A. A. Pilla.* Each coil had a radius of 6.4 cm and was constructed of 60 turns of 16 gauge magnet wire. Also, the distance in the z direction separating the coils was equal to the radius of the coils (Helmholtz spacing [12]). Systems of this type are presently used clinically to heal nonunion bone fractures. The system induced waveforms shown in Figure 4 with a repetition rate of 72 Hz.

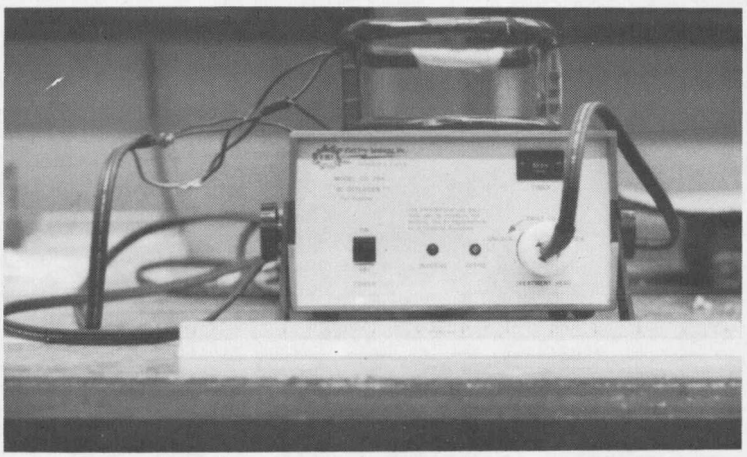


Fig. 3. DCS.

Figure 2 illustrates (actual scale) a coil of the DCS as well as coils used as inductive test systems (ITS's). It is apparent that the DCS coils were not round. Therefore, the assumption that only the E_ϕ component of $\bar{E}$ exists was not exactly correct. However, it is

*Model CU-204 BI-OSTEOGEM T.M., pat. pending, manufactured by Electro-Biology Inc., Fairfield, N.J., U.S.A.

pointed out that the geometry and symmetry of the coils was such that the assumption of only a ϕ component of $\bar{E}$ was not unreasonable. Thus, it was believed that measurements taken using the DCS would still be valid to verify the theory for round coils.

While the mutual inductance of the two coils of the DCS was considered to determine the current in the DCS coils, any effects of the mutual inductance created by the ITS were ignored. This is to say that changes in spatial variations were assumed due to the positioning and size of the ITS, and not due to a change in mutual inductance term caused by DCS/ITS interaction. This assumption was validated through measurements of circuit parameters of the system. Inductance values of the ITS's ranged from 2 to 7 microHenerys. Also, the total inductance of each of the coils of the DCS was found to be 980 microHenerys (method of determination in Appendix D). All values of inductance were measured on an inductance bridge at a frequency of one kiloHertz. With the coefficient of coupling (k_c) approximately 0.15, it was concluded that the change in the current of the DCS as well as the field distortions caused by the interaction of the ITS and the DCS were negligible. An examination of Table 1 clarifies this issue. Here values of the $\partial I(t)/\partial t$ for two ITS's are displayed.

Table 1. Values of $\partial I(t)/\partial t$ for Different ITS's.

r_{ITS} cm.	E_ϕ mvolt/m	L_{ITS}	M_{ITS}	L_T	$\partial I(t)/\partial t \,_{t=t_1}$
2.0	50	2.0	6.6	973	11,600
5.1	120	4.0	9.4	970.6	11,630

$M_{ITS} = k_c \sqrt{L_{ITS}(980)}$; $L_T = 980 - M_{ITS}$; all inductance values are in microHenerys; $t_1 = 0.1$ msec and units of $\partial I(t)/\partial t$ are amperes per second. Also, methods for determining $\partial I(t)/\partial t$ as well as other parameters are in Appendix D.

The equation used to determine $\partial I(t)/\partial t$ was

$$V(t) = L_T \partial I(t)/\partial t + RI(t) \qquad (12)$$

Figures 42 and 43 (Appendix E) indicate that V(t) did not change for the different ITS's. Further, Table 1 shows that although the values of E_ϕ changed by more than 100 percent the value of the $\partial I(t)/\partial t$ changed by only 0.3 percent. Now since the $\partial I(t)/\partial t$ is the only part of Equation 6 that could have been altered by a change in mutual inductance it was concluded that the mutual term between the ITS and the DCS could be ignored. Therefore, the changes in EMF were due to changes in field strength as a function of space and these changes were measured by a specific orientation of the ITS.

EMF's used to calculate E_ϕ were measured using various sizes of ITS's consisting of 23 gauge magnet wire centered at the origin in a constant z plane. An example ITS is pictured in Figure 2. E_ϕ was made constant with respect to integration by using different sized current loops each with fixed radius and each centered at the radial center of the DCS, as a source of the EMF. The values of r_1 of Figure 2 corresponds to the values of r in Figures 6-10. Measurements of the EMF were taken using a Tektronix type 454A oscilloscope and all values of E_ϕ were calculated for $t_1 = 0.1$ millisecond. It is mentioned that this method realized a value of E_ϕ for the positive portion of the pulse and that E_ϕ for the negative portion of the pulse is larger in magnitude, opposite in sign and shorter in duration but the two will be proportional. The method used to calculate the EMF at t_1 was to measure v_1 as shown in Figure 5 and then multiply by the value of the exponential decay at time t_1. Assuming the exponential decay to vary only slightly for different ITS's, only one calculation of the time constant was made. Finally, the experimental value of E_ϕ

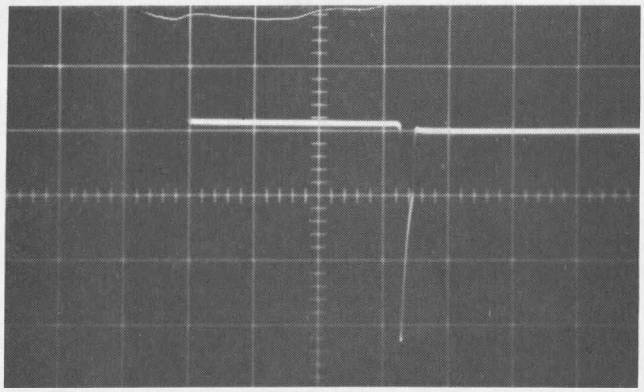


Fig. 4. Total EMF of ITS, E_ϕ Type, r of ITS = 4.6 cm Vertical Scale 500mv/cm, Horizontal Scale 0.1 msec/cm.

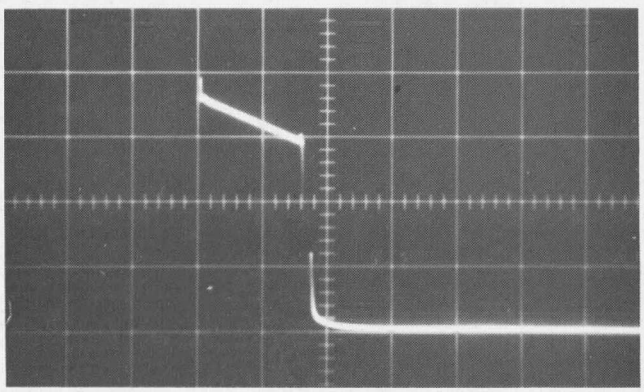


Fig. 5. Positive Portion EMF of ITS, E_ϕ Type, r of ITS = 4.6cm Vertical Scale 20mv/cm, Horizontal Scale 0.2 msec/cm.

was calculated by dividing the value of the EMF at t_1 by $n2\mu r_1$; n and r_1 being the number of turns and the radius of the ITS respectively.

A small ITS was used to measure EMF's to calculate B_z and its location was altered in order to find the spatial variation of B_z. Sixteen circular turns with a radius of 0.38 centimeters of 23 gauge magnet wire composed the ITS. EMF's measured in a constant z plane at a particular r_2 as in Figure 2 were used to calculate the value of B_z at r_2 and t_1. An example of this process is given in Appendix F.

Theoretical and Experimental Results

Experimental values of E_ϕ and B_z were plotted and are displayed in Figures 7 and 9. When compared to the theoretical plots of Figures 6 and 8 it can be seen that the experimental values confirm the theoretical predictions and an RMS error analysis is included in Appendix K. Also, the experimental values at z = 2 cm for E_ϕ are less than the theoretical values because the coils were not round; thus effectively causing portions of the source, DCS, to be further from the field point, ITS, than the theory dictates.

From these plots it can be concluded that a biological system will be exposed in uniform B_z provided that the following criteria are met. First, the biological container should be centered at the DCS origin, i.e., z = r = 0 in Figure 1. Second, the dimensions of the container should not allow cells to be exposed beyond r=4 cm, i.e., 60 percent of the DCS radius in general, in order to stay in the region of constant B_z. Finally, it is apparent from Figures 6-9 that B_z varies in the z direction for fixed r; however, B_z will remain nearly constant within the r=4 cm range provided the systems z dimensions are ± d (see Figure 1) with d=2 cm for these coils. Further research is needed in order to determine total B_z vari-

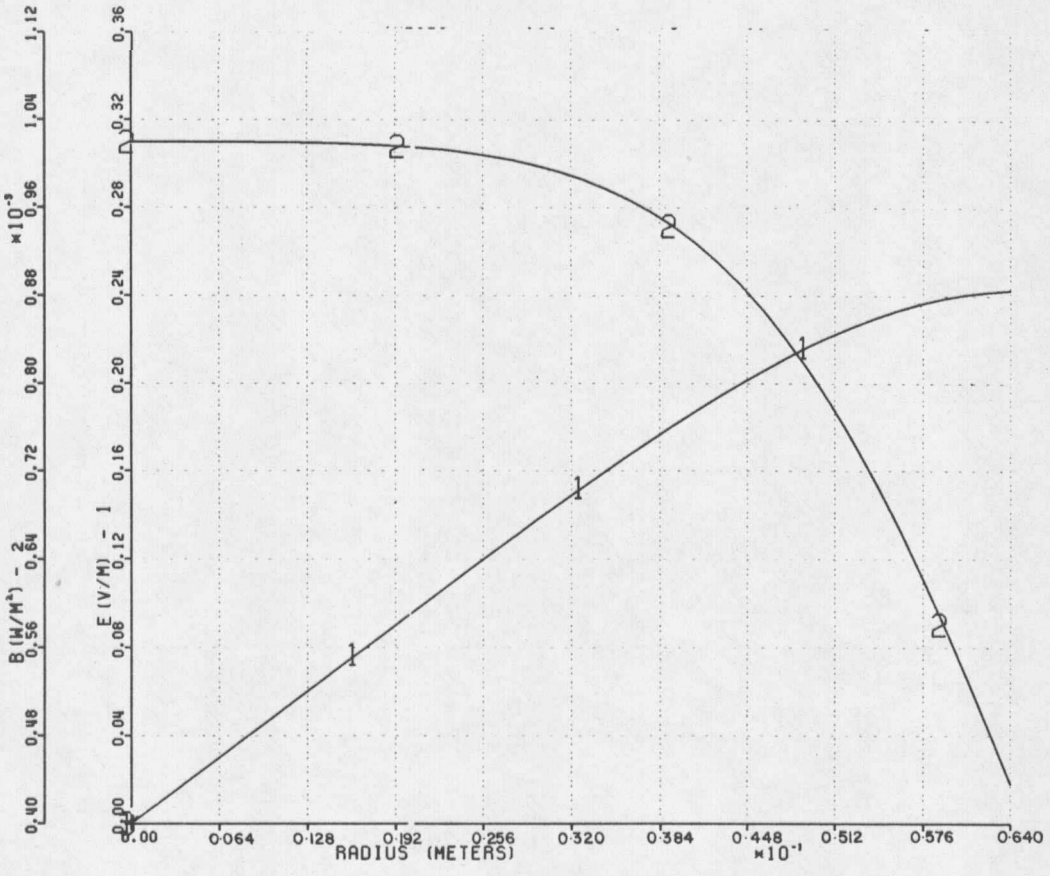


Fig. 6. Theoretical Fields, z = 0 Plane, t = 0.10 msec.

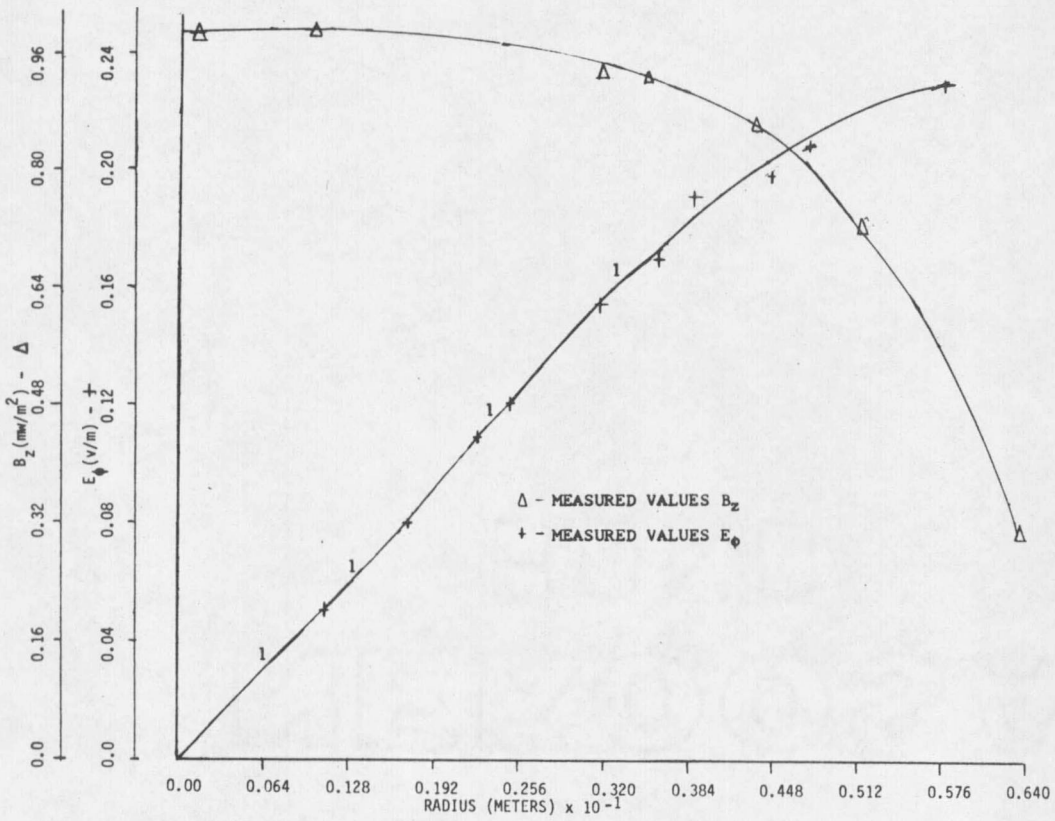


Fig. 7. Experimental Fields, z = 0 Plane, t = 0.10 msec.

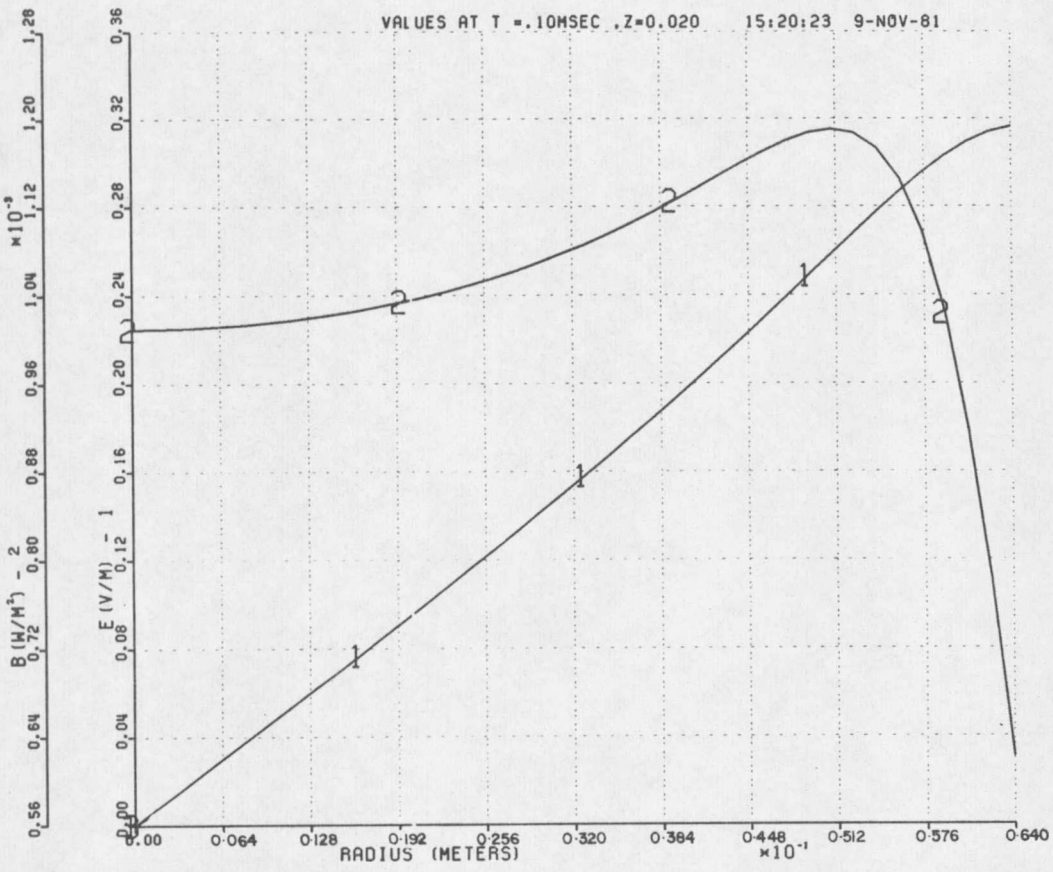


Fig. 8. Theoretical Fields, z = 2cm Plane, t = 0.10 msec.

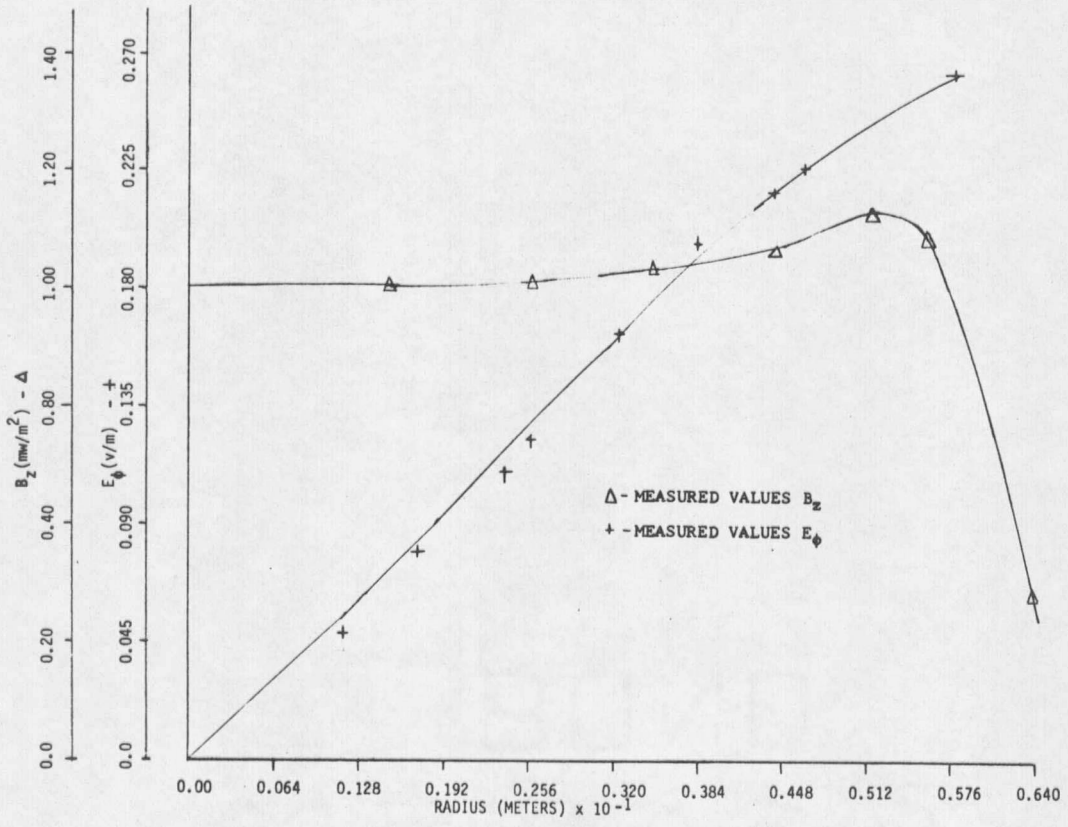


Fig. 9. Experimental Fields, z = 2cm Plane, t = 0.10 msec.

ations with z. Following all of the preceding criteria would, however, ensure that the cells would be exposed in a constant B_z. Further, B_r is nearly zero under the above criteria and although B_r was initially neglected in this study there are areas between the coils where B_r is significant. However, the drawback is that E_ϕ would vary markedly where B_r is zero and the plots obtained for free space can be used to determine E_ϕ (variation not magnitude) if and only if the preceding criteria are met with a cylindrical container exposed to the coils as shown in Figure 19. Different orientations and boundary conditions are discussed in Chapter III.

Accuracy of Results

First, the assumption that only a phi component of $\bar{E}$ existed was not totally correct. However, as mentioned before this assumption was reasonable. Second, B_z was assumed constant in a specific region and was therefore pulled out of the integration. This process was extended for experimental values to the regions where the theoretical plots predicted B_z was not constant. Therefore, only an estimate of experimental B_z could be obtained in this manner: with the estimate being plotted for comparison with the theoretical plots. Finally, EMF measurements taken with the ITS's were repeatable to within 2 and 10 percent for E_ϕ and B_z type ITS's respectively. B_z measurements were more variant because the test system was hand-held in position and it was difficult to keep $\bar{ds}$ exactly parallel to B_z.

Chapter II

FOURIER ANALYSIS

Fourier analysis of a burst type waveform was done on a digital computer in the hope of discovering why different repetition rates of the waveform caused different biological results. A paper by Pilla [5] stimulated this work. Pilla indicated biological systems exposed to the induced waveforms could have dramatically different results based on only the change of repetition rate of the waveform. Percent change versus control ranged from largely positive for a 15Hz rate to slightly negative for a 5Hz rate. Thus, power spectral plots of 5, 11, 15 and 20Hz (rates used in Pilla's work) were obtained in an effort to explain the differences. When initial work proved insufficient to answer the question, the Fourier work was deferred to a latter and more complete study. However, the efforts that were taken are described.

A digital computer program (FOURIER in Appendix B) was used to compute the Fourier series of burst type waveforms with different repetition rates. The equation used to determine the series

$$f(t) = \sum_{n=0}^{\infty} a_n \cos(\omega_n t) + b_n \sin(\omega_n t) \qquad (12)$$

contained sinusoid basis functions. The components a_n and b_n were used to determine the magnitude of the voltage spectrum at their corresponding frequency (f_n). An approximation of the burst type waveform, f(t), can be seen in Figure 10. It was assumed the actual shape of the individual pulses of the wave form was similar to the shape of the pulse in Figure 4. Such an approximation dictated both equal area and equal energy in the positive and negative portion of the pulse (see Appendix I). Spectral plots for the 11, 15 and

20Hz repetition rates are shown in Figures 14-16 and although the spectrum for the 5Hz waveform is not included in the figures its components were also examined. Voltage components obtained by

$$V_n = (a^2{}_n + b^2{}_n)^{1/2} \tag{13}$$

were plotted versus frequency (the scaling factor of square root of one-half was not included, i.e., the magnitude of all spectral values should be multiplied by square root of one-half to obtain actual values). It was the hope of the author that the spectral envelope of the burst was unique enough that a noticeable difference would occur in a specific frequency range of the voltage spectra of the negative versus positive biologically effective repetition rates. This would have suggested a resonance effect in the biological system. This did not prove to be the case; Table 2 was created in order to examine this point. Here the magnitudes of the spectra are compared at specific frequencies. Only the "main components" as shown in Figure 14 were compared. An inspection of Table 2 shows that the relative magnitudes of the various repetition rates can be made equal by normalizing the magnitudes for each repetition rate. This normalization process was done by dividing the component by its repetition rate. Upon completion of the normalization it can be seen that all values at like frequency are approximately equal. Thus, it was concluded that the relative magnitude of the spectra increased proportionally to the repetition rate and the spectral envelope of the pulse train was not unique enough that any appreciable difference in the areas of the significant components were observed for the various rates. This is to say that although there are fewer harmonics and the magnitudes of the harmonics are larger as the repetition rate increases this occurs throughout the frequency range. Therefore, it was concluded that this method of analysis could not reveal frequency regions where the

relative amount of energy of one waveform varies significantly from the others. True, all waveforms have different amounts of energy over the same frequency range but the difference is proportional throughout all frequencies of the spectrum as should have been suspected. Although the results do not refute a possible resonant effect they do nothing to support that claim.

Table 2. Main Components for Various Repetition Rates.

	Component magnitudes versus frequency for various repetition rates			
Frequency (kHz)	5 Hz	11 Hz	15 Hz	20 Hz
4.4	0.050	0.110	0.148	0.200
8.8	0.047	0.105	0.148	0.185
13.2	0.043	0.095	0.132	0.175
17.6	0.039	0.058	0.132	0.159
22.0	0.034	0.085	0.119	0.135
26.4	0.028	0.062	0.085	0.112

Also, a Fourier transform (Figure 13) of an approximation of the single pulse of Figure 4 was done using a hand-held calculator. The approximation of the waveform used to find the transform is displayed in Figure 11 and the negative portion is enlarged (time scale) in Figure 12. It is pointed out that the approximate waveform contained more energy at the higher frequencies than the actual waveform. This point is supported by noting the abrupt edges of the approximation versus the actual waveform (Figure 18) at the maximum point of the negative portion of the pulse as well as at the zero crossing. Also, an examination of a lowpass (LP) filter output of the negative portion of the waveform (Figure 17) shows that the lower cut off frequency smooths the time function. Thus, it is concluded that the approximation of the actual waveform contained more high frequency energy than the actual waveform.

When spectral outputs of the approximate burst waveform as well as that of the approximate pulse and lowpass filter outputs are examined, the same conclusion is reached: there were no significant frequency components above the one megaHertz range. An examination of Figure 13 demonstrates this for the single pulse and Figures 17 and 18 indicate the lowpass results. Further, Appendix G figure shows a single pulse of the burst waveform which was obtained using the first 10,000 components of the Fourier series. Since the waveform was fairly well duplicated, ignoring Gibb's phenomenon and since the upper limit of the 10,000 component is 200 kHz (for 20Hz repetition rate) it can be seen that the pulse waveform of both the single pulse and the burst type waveforms contained no significant energy above one megaHz.

Current Density a Result of Fourier Analysis

That there was no energy above one megaHz in the waveforms used to modulate the biological systems leads to the following results. From Maxwell's fourth equation

$$\nabla \times \bar{H} = \bar{J} + \partial \bar{D}/\partial t \qquad (14)$$

an examination shows that the $\partial \bar{D}/\partial t$ can be ignored if: first, no significant energy occurs above one megaHz, and second, the permittivity constant ($\epsilon_o \epsilon_r$) of the biological system is small and not a rapidly varying function of time. The first condition is made assuming ϵ_r of biological systems to be of the order of 200; however, when ϵ_r is large (10^4 or greater) the $\partial \bar{D}/\partial t$ cannot be ignored for all frequencies below one megaHz. Since $\bar{J}$ is equivalent to $\sigma \bar{E}$ and σ is known to be approximately one moh/meter [13], a value of ϵ_r of up to 200 would still allow $\partial \bar{D}/\partial t$, or $\epsilon_o \partial \epsilon_r \bar{E}/\partial t$, to be neglected for all frequencies below one megaHz. With ϵ_r equal to 200, $\epsilon_o \epsilon_r$ is of the order of 2×10^{-9} and the time derivative factor

at one megaHz, i.e., 10^7, is not large enough to make $\partial \bar{D}/\partial t$ significant compared to $\sigma \bar{E}$. However, if ϵ_r were time dependent another term should be considered. Still the time variance of ϵ_r would have to be prohibitively large before the $\partial \bar{D}/\partial t$ becomes significant; thus, for values of ϵ_r less than 200 the type of current affecting the biological systems modulated by the burst type as well as single pulse waveform is $\sigma \bar{E}$. Should ϵ_r become large (10^4 or greater) the $\partial \bar{D}/\partial t$ could have a significant effect at the higher frequencies of the waveforms.

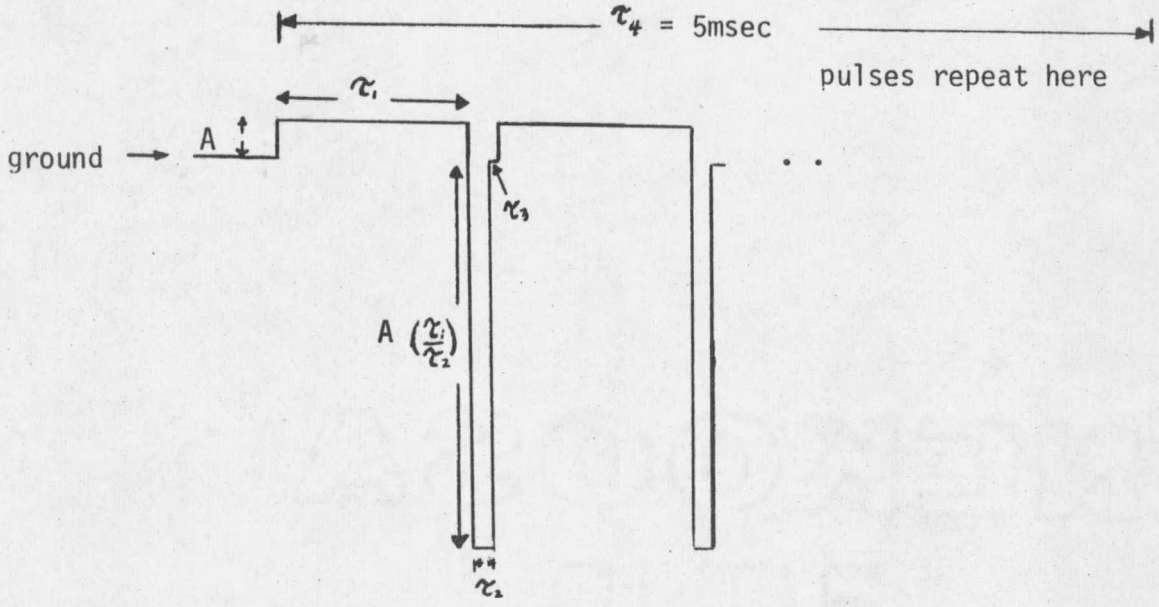


Fig. 10. Square Wave Approximation of Burst Used in FOURIER. τ_1 = 200microsec, τ_2 = 20microsec, τ_3 = 8microsec and at the end of τ_4 back to ground until the burst repeats at the specific repetition rate.

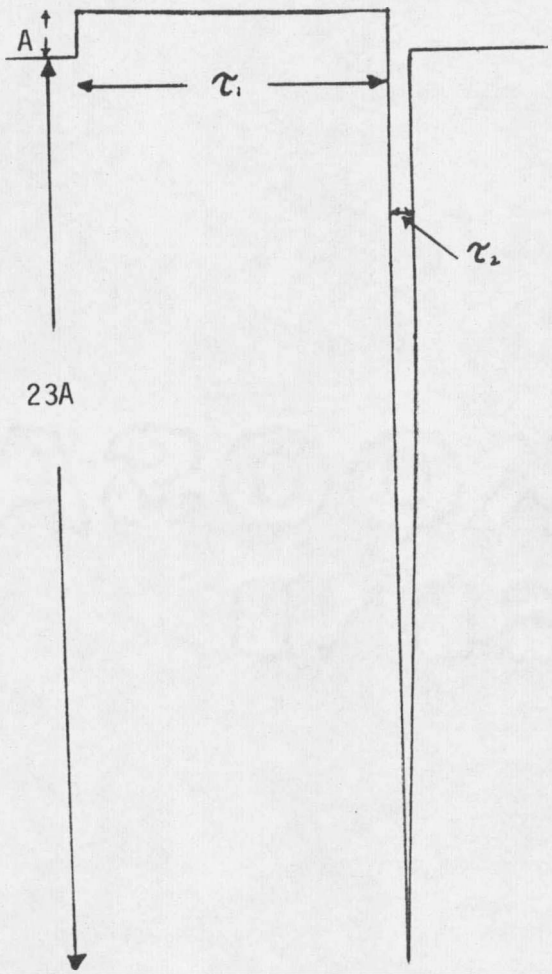


Fig. 11. Approximation Single Pulse Waveform Used to Find the Voltage Spectrum of Figure 13 (see Appendix H for details).

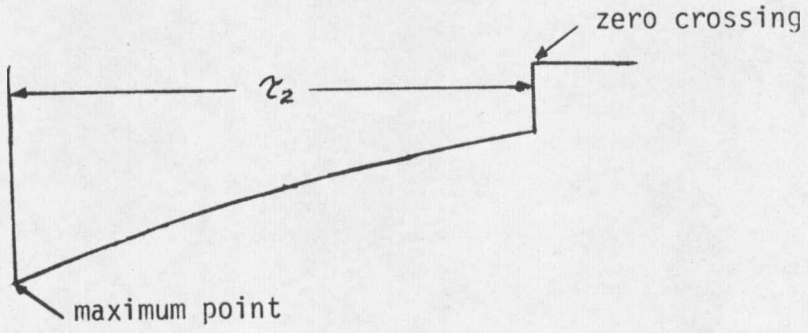


Fig. 12. Enlargement of the Negative Portion of Figure 11.

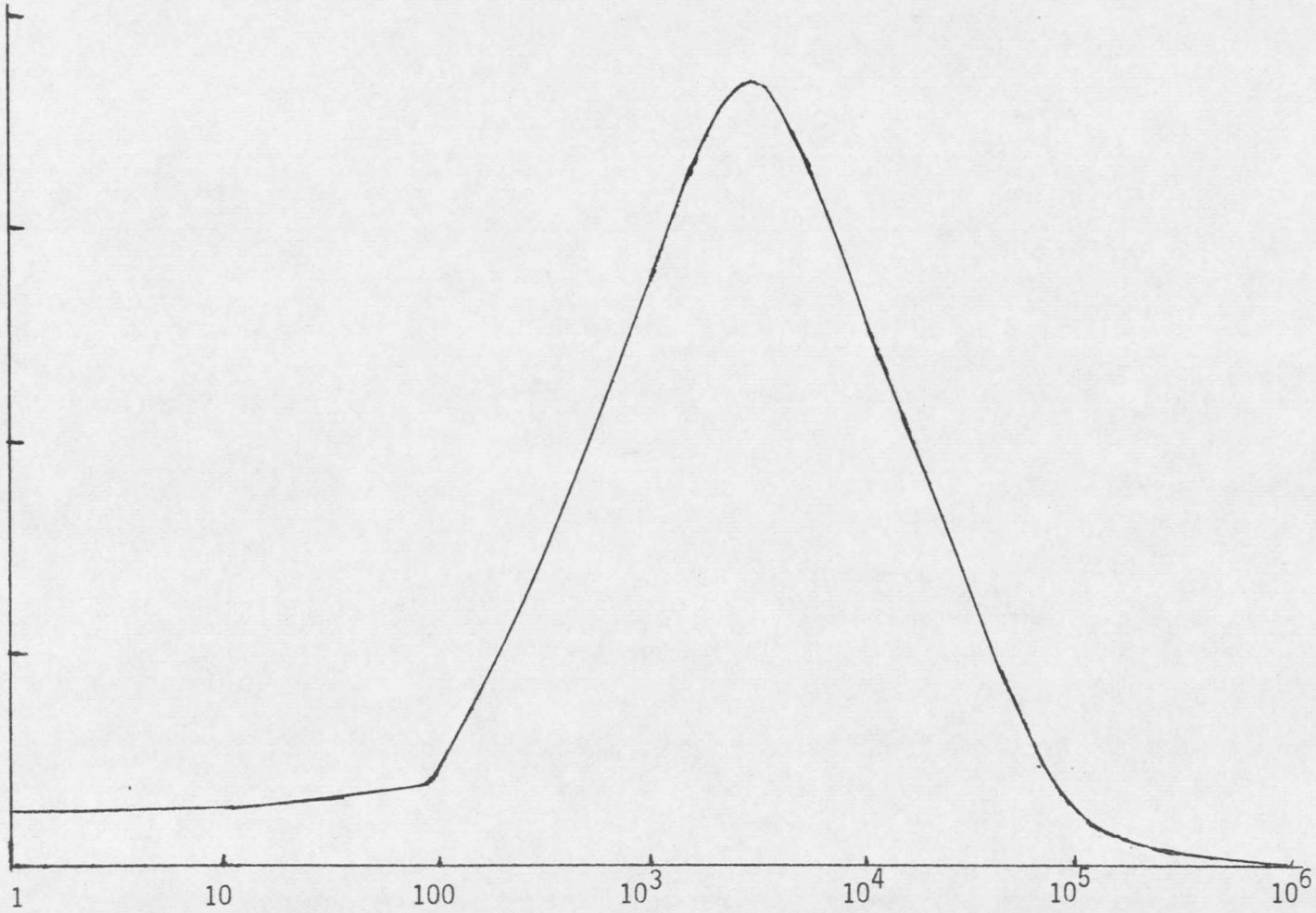


Fig. 13. Voltage Spectrum of Figure 11 (see Appendix H for details). Horizontal Scale Logrithmic Hz, Vertical Scale 100 volts per Division.

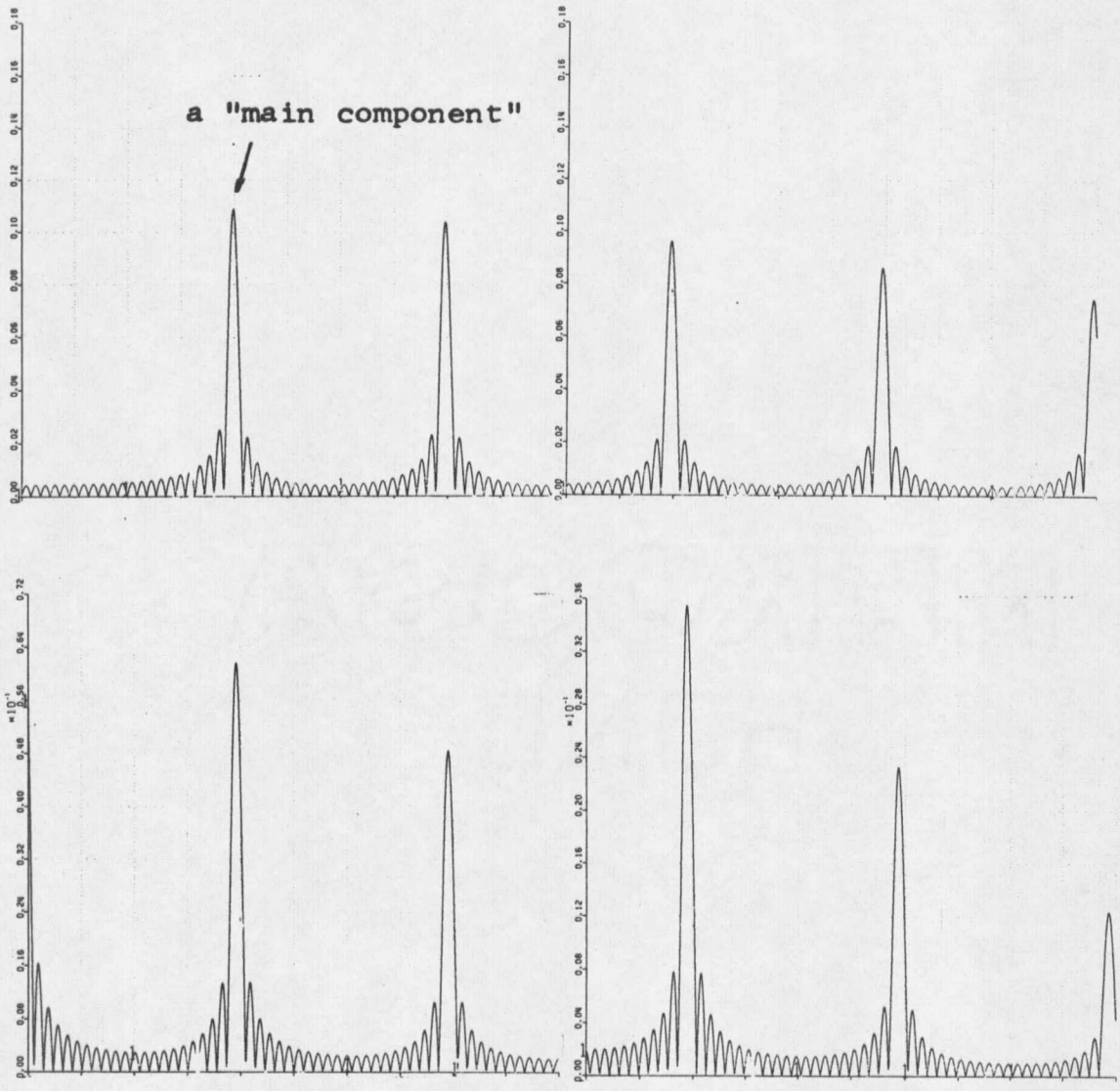


Fig. 14. Voltage Spectrum 11Hz Burst Waveform Where Vertical Scales Vary in Magnitude. Horizontal scale 1.1kHz per Division.

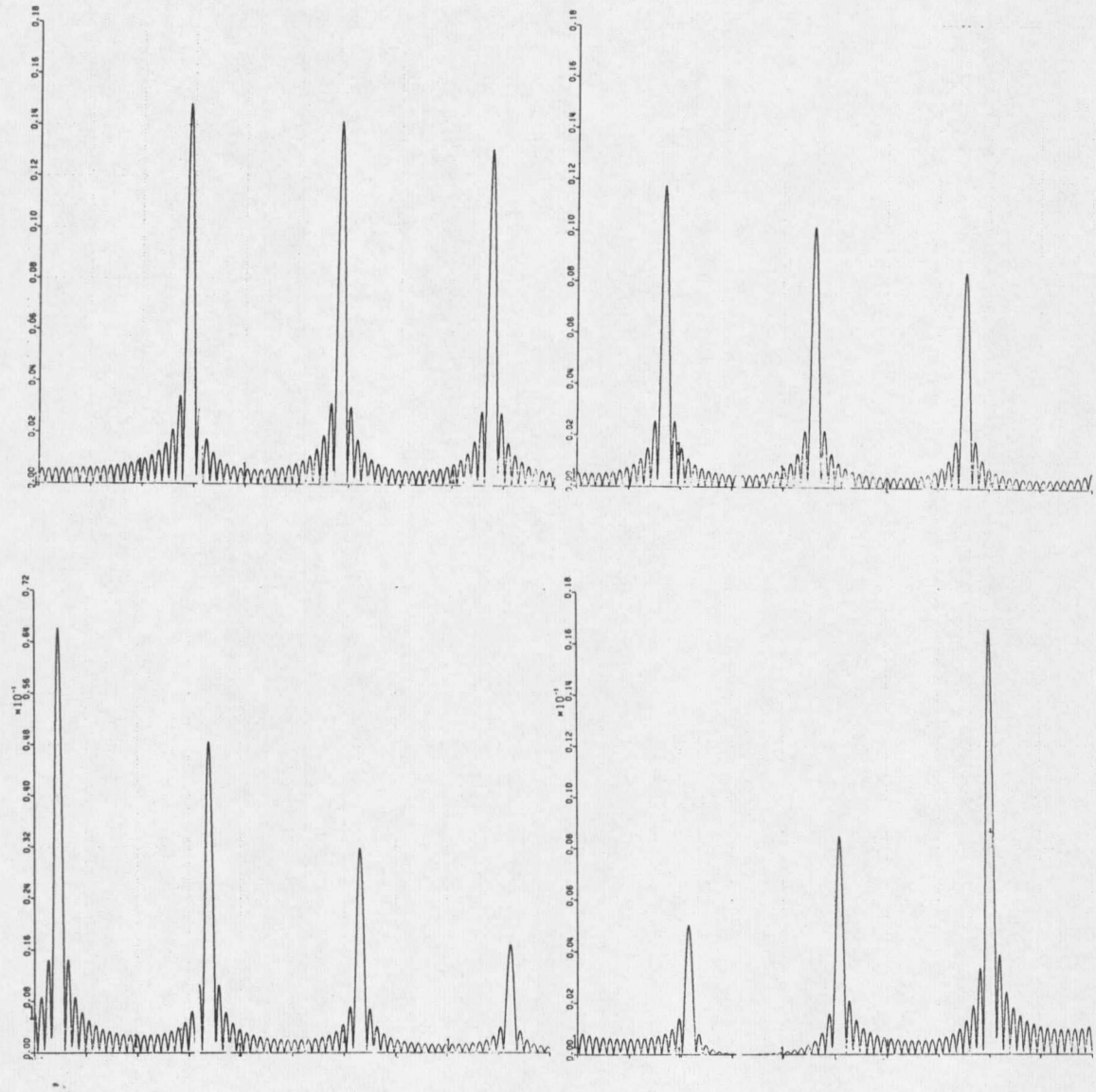


Fig. 15. Voltage Spectrum 15Hz Burst Waveform Where Vertical Scales Vary in Magnitude. Horizontal scale 1.5kHz per Division.

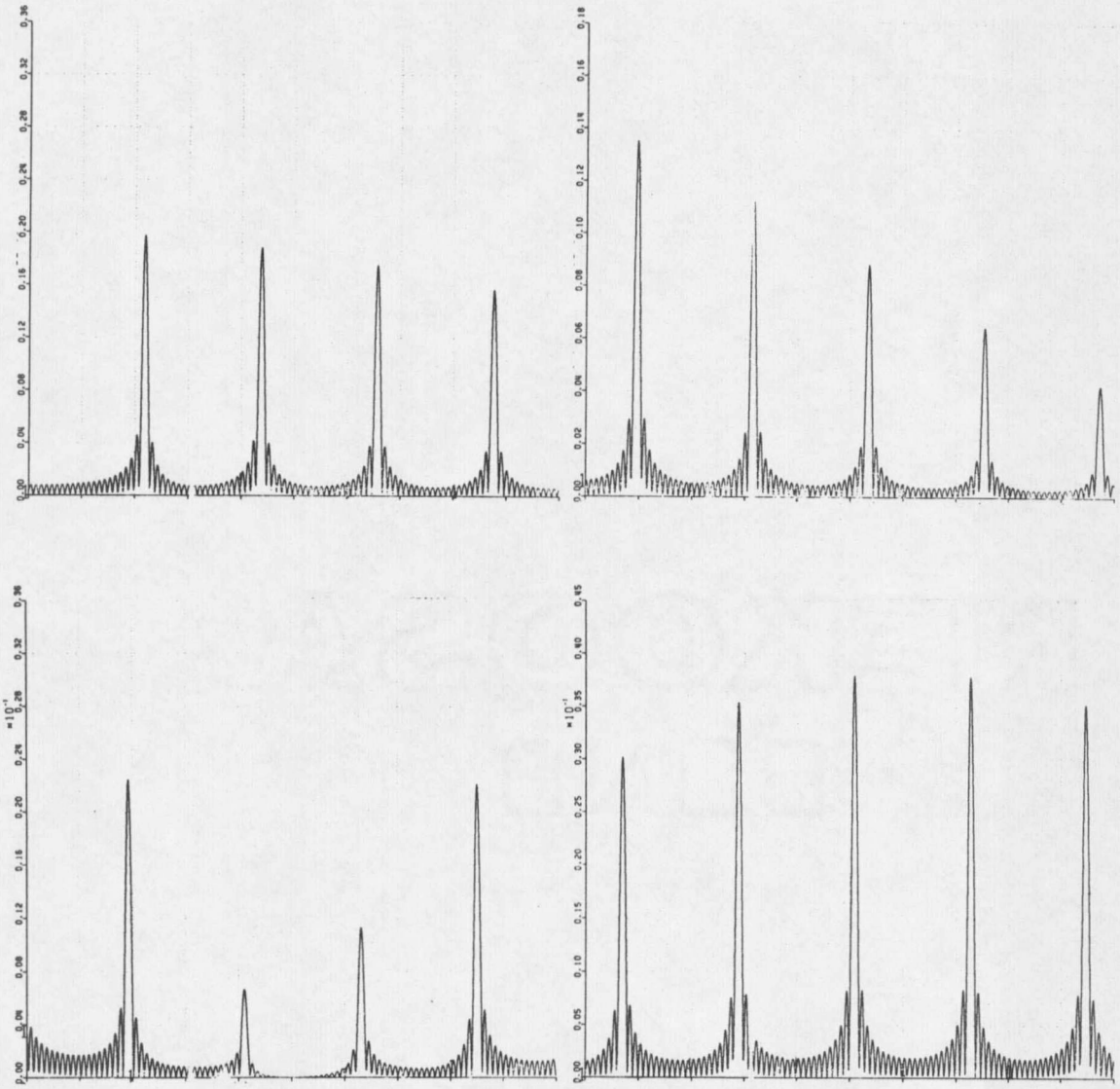


Fig. 16. Voltage Spectrum 20Hz Burst Waveform Where Vertical Scales Vary in Magnitude. Horizontal scale 2.0kHz per Division.

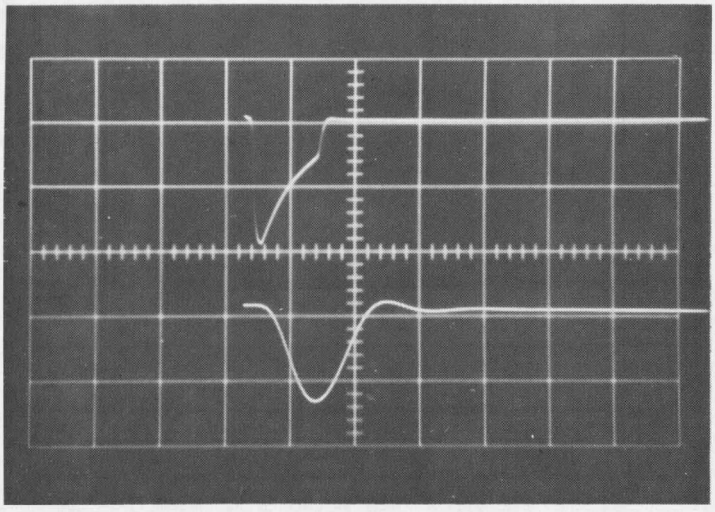


Fig. 17. LP Output (38kHz) Upper Trace Unfiltered Wave, Lower Trace Filtered Wave, Horizontal Scale 20microsec per Division.

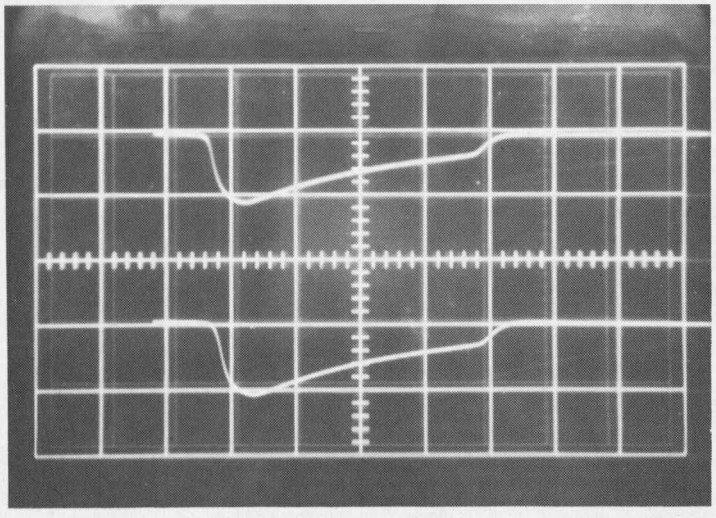


Fig. 18. LP Ouput (one megaHz) Upper Trace Unfiltered Wave, Lower Trace Filtered Wave, Horizontal Scale 5microsec per Division.

Chapter III

BOUNDARY CONDITION CONSIDERATIONS AN EXPERIMENTAL VIEW

Although spatial variations of E_ϕ and B_z in Figures 6-9 describe the field variations in free space, caution must be used in applying these values for various DCS orientations as well as various boundary conditions. Orientations of the DCS considered are displayed in Figures 19 and 20. Experimental boundary conditions were set up that consisted of a cylindrical glass beaker and a rectangular plexiglas box. Ringer's solution was used as the conducting media in all tests and was prepared as follows:

8.7 g salt (NaCl) per liter water

The following work was done in an effort to describe fields external to the cell at various positions inside the bounds of the salt solution.

Experimental Procedure

Spatial variations of $\bar{E}$ for the two orientations and containers were measured by the following apparatus. Two 2.5 mm 23 gauge magnet wire leads served as a dipole antenna which was submersed in the Ringer's solution at selected positions. Leads from the dipole were twisted for noise suppression, i.e., ideally no extraneous signal was induced between the dipole and the operational amplifier. This was done assuming any signal induced on one of the twisted wires would also be induced on the adjacent twisted wire. Small signal levels necessitated an operational amplifier which was used as a difference amplifier so that any noise signals of like sign and equal magnitude at the amplifier inputs would be eliminated. Upon amplification the signal was observed using a Textronix 454A oscilloscope. To

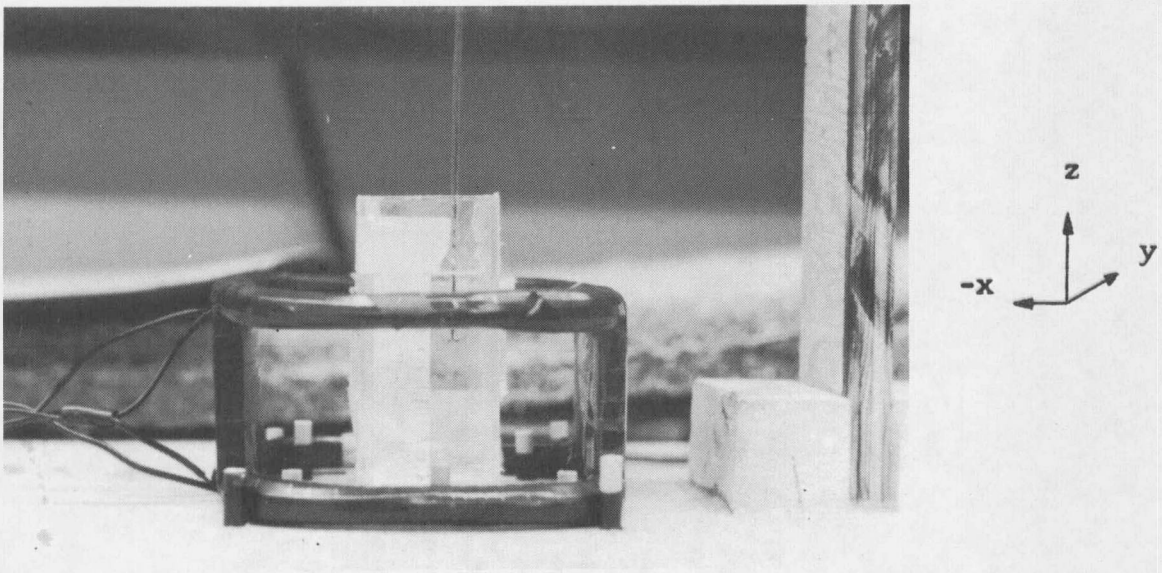


Fig. 19. DCS Horizontal.

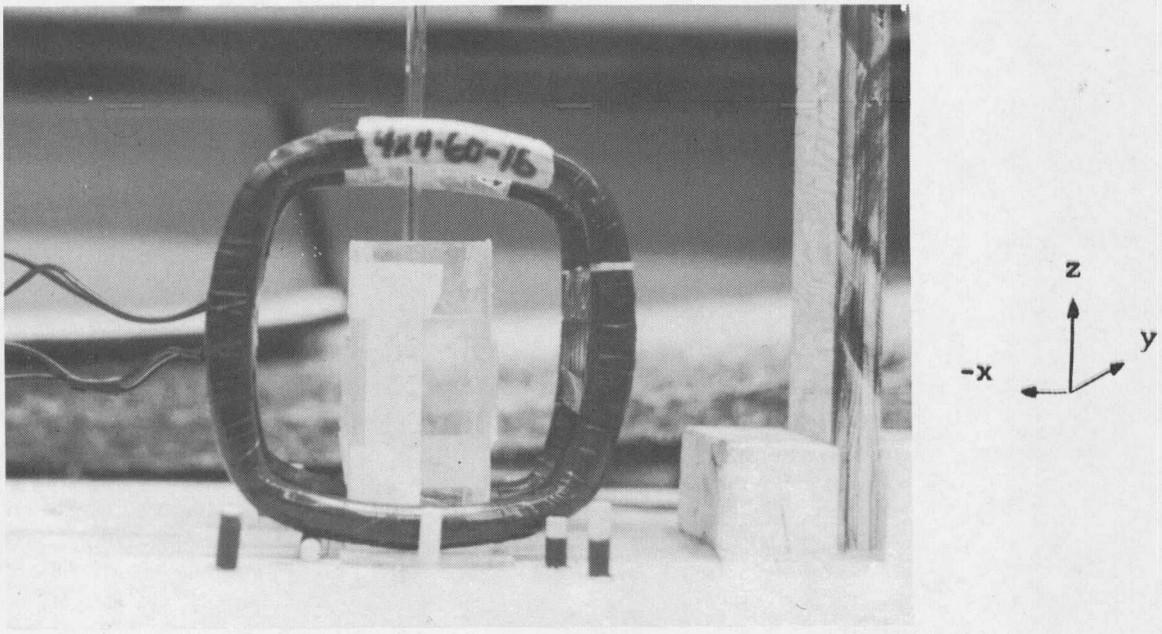


Fig. 20. DCS Vertical.

obtain sufficient signal strength measurements were taken from the negative portion of the pulse (as opposed to the positive portion of the pulse used for the free space measurements). It is not to be concluded that the signal level was significantly lower than those in free space; however, the dipole provided much less gain than the previous ITS's. Gain of the dipole is not considered and all values plotted in this chapter were taken directly from the oscilloscope readings, i.e., the reading of the maximum point of the negative pulse was plotted; no conversion to actual field magnitudes was done. This was sufficient since for this work only relative magnitudes were needed.

Signals were measured at the positions shown in Figures 22 and 23 for the rectangular and cylindrical boundaries respectively at a specific z plane. This was done by centering the dipole at the points and orientating the dipole to obtain E_x or E_y. Ideally the dipole was to pick the $\bar{E}$ component tangential to it and reject the components normal to it as shown in Figure 21. Here E_x would be measured and E_y rejected. Also, it can be seen than tangential components would provide signals of equal and opposite magnitude relative to the difference amplifier; thus, the signals due to tangential components will add at the amplifier.

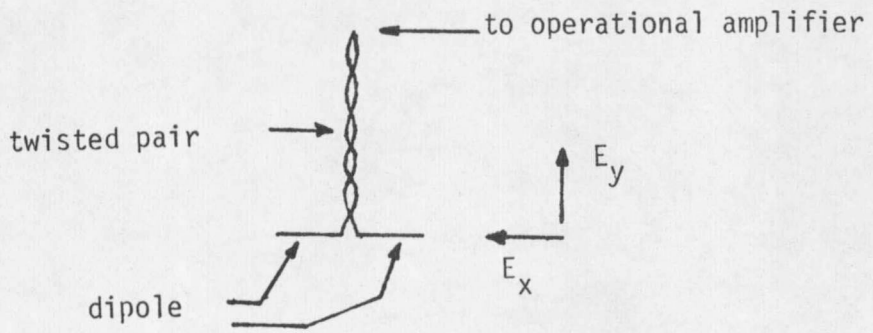
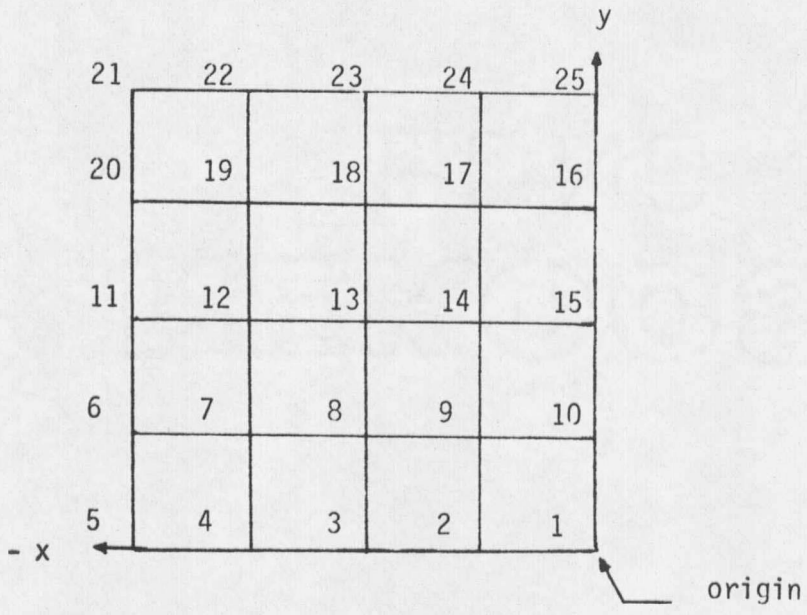


Fig. 21. Dipole Fields Measured.



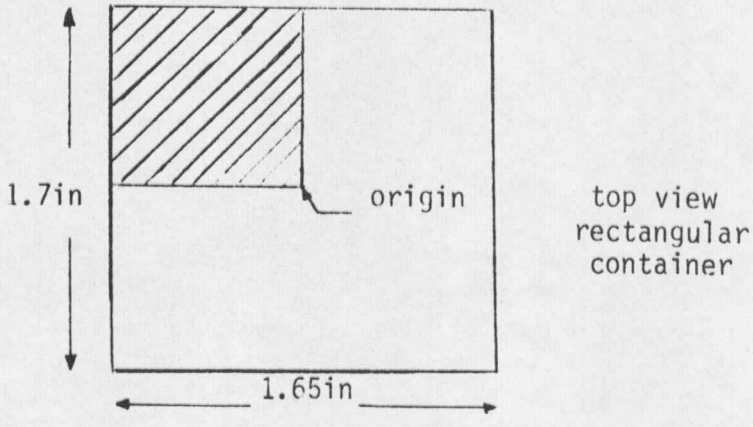


Fig. 22. X,Y Positions Coils Horizontal Where Numbered Region Corresponds to Crossed Region. Symmetry Dictates Only One Fourth of the Area Need be Measured.

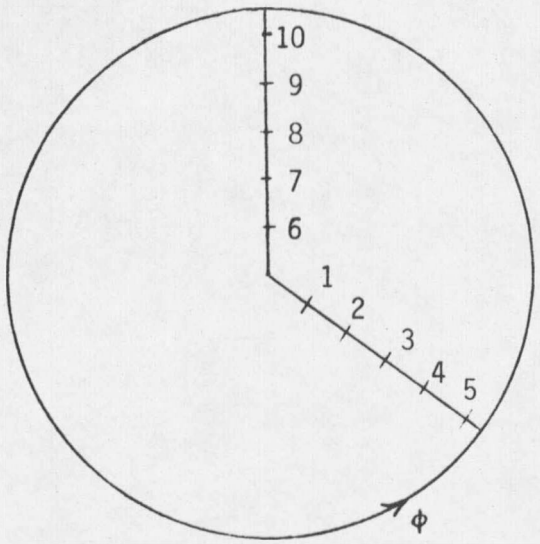


Fig. 23. Cylindrical Positions Coils Horizontal Where Values of E at Positions 1-5 Correspond to the Values at 6-10, i.e., E_ϕ Varies With r, Constant With ϕ.

Experimental results confirm the dipole hypothesis. Theoretical solutions for $\bar{E}$ are shown to contain only E_ϕ [14] for the orientation shown in Figure 19 with a cylindrical container. Since attempts to measure E_r (see Fig. 1 for r) yielded a near zero reading it was assumed that the dipole functioned as was intended. Recall that for this orientation and boundary only an E_ϕ component exists and the r direction is always normal to ϕ.

Figures 24-26 show that the waveform varied proportionally at the specific positions of measurement of Figure 22, i.e., both the positive and negative portions of the pulse increased or attenuated at different positions. This result shows the approximate linearity of the measurement system.

A crude stage was built in order that the measurements would have some consistency. The twisted wire was held firm by a glass tube which was positioned such that the dipole would be centered at a desired position of measurement. Errors in measurement occurred

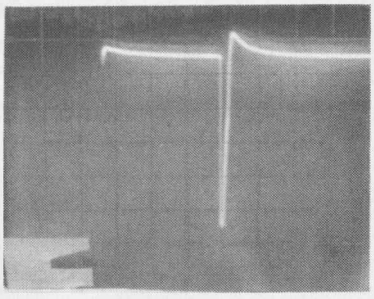


Fig. 24. Dipole EMF Position 14, z=0 Coils Horizontal.

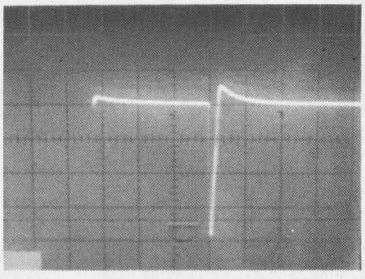


Fig. 25. Dipole EMF Position 25, z=3.5 cm, i.e., 3.5 cm Above z=0 Coils Vertical.

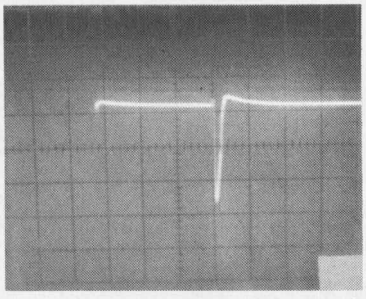


Fig. 26. Dipole EMF Position 25, z=2.3 cm, i.e., 2.3 cm Above z=0 Coils Vertical.

due to diffraction and parallax effects as well as the inability to orient the dipole such that only the exact desired tangential component was measured.

Experimental Results

Horizontal Orientation

The field map for the positions of Figure 21 is shown in Figure 28. In this figure and all which follow only the relative value of E has been plotted, i.e., values read directly from the oscilloscope were plotted at proper positions. Four sets of data were taken in the rectangular box in the x,y plane located at z = 0 and the 'Student's' t test was performed on the data. Results of the test are displayed in Appendix J. It became too involving to obtain 4 sets of data for all plots: therefore, only two sets of data were taken for the remaining plots. Since two sets of data would not provide valid statistical tests no further statistical tests were performed. Each data point is the average of the measured values.

Although the z = 0 plane is displayed in Figure 1 it is repeated here for convenience in Figure 27. The box as well as cylinder were filled with 3 in. water in the horizontal orientation (Fig. 19). Further, the origin of the DCS corresponds to the origin of the container (see Figs. 1 and 22 respectively).

The field variations for the cylindrical boundary are displayed in Figure 29. Here oscilloscope readings are plotted versus r because a ϕ component of $\bar{E}$ existed and E_ϕ was constant with ϕ. Obviously E_ϕ varies linearly with r as the theory says it should.

From Figures 28 and 29 it can be seen that both containers created boundary conditions which forced $\bar{E}$ to vary at particular positions within a constant z plane. Although not confirmed it was assumed that the same relative variations of E_x and E_y or E_ϕ versus

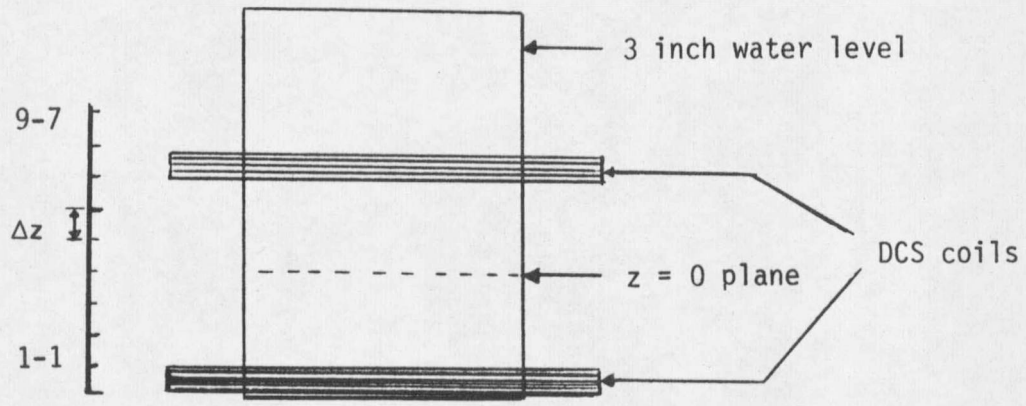


Fig. 27. z Positions Both Containers Coils Normal.

the positions of Figures 28 and 29 respectively were present at different constant z planes. Data which support this assumption is shown in Table 3.

Table 3. Relative Changes in E_x for x,y Positions, Horizontal Orientation.

	Rectangular Container			Cylindrical Container		
	x,y Positions	16	17	x,y Positions	16	25	
1		64	57		56	68	1
2		64	56		56	68	2
3		63	55		56	68	3
4		62	55		55	67	4
5		60	54		54	66	5
6		59	53		53	66	6
7		58	53		53	65	7
8		57	53				
9		56	51				

Both positions 1 for round and rectangular boundaries correspond to position 1 in Figure 27 and the Δz is 0.23 in. and 0.25 in. for the rectangular and cylindrical boundaries respectively. Also, the x,y positions correspond to Figure 22 where the cylindrical containers radius was approximately at position 25.

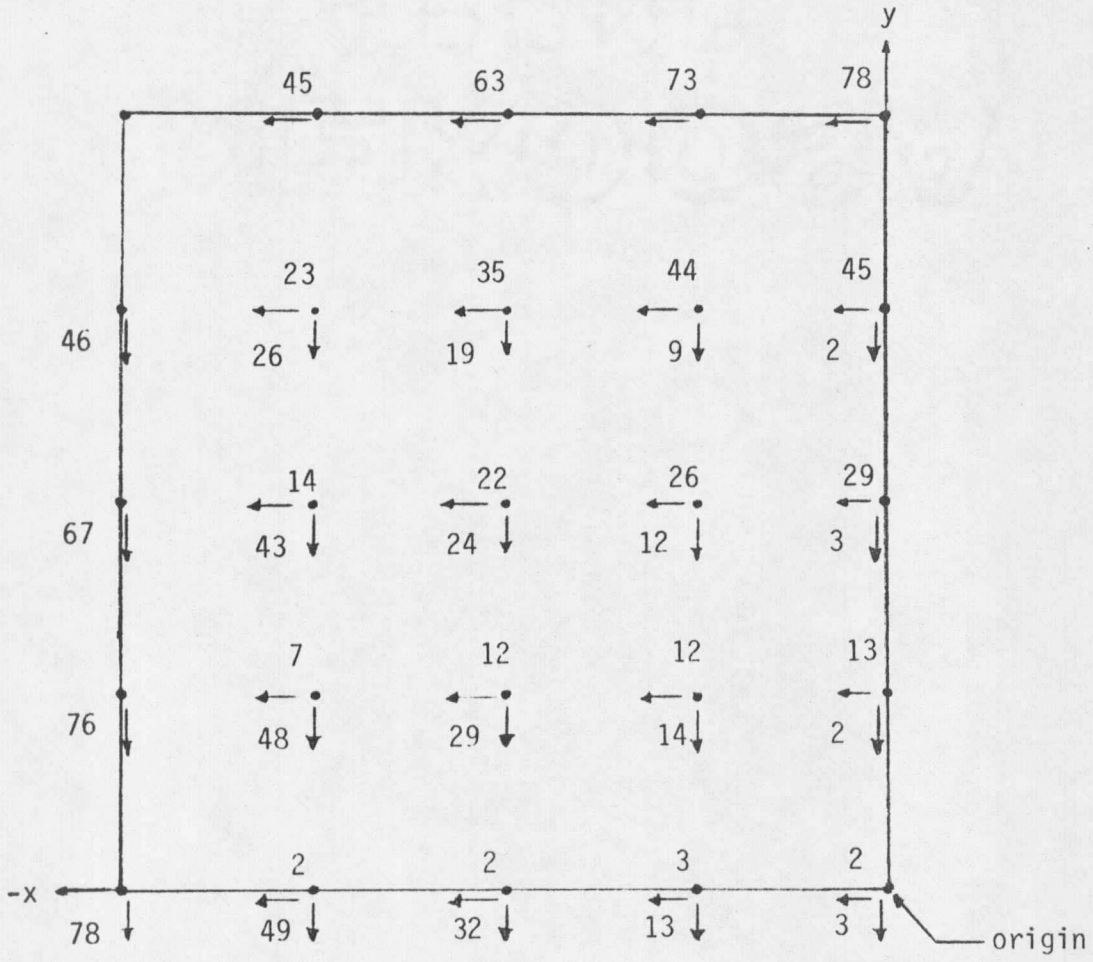


Fig. 28. Field Plot for Positions of Figure 21 Certain Positions Not Measured Due to the Physical Dimensions of the Dipole. Numbers above points correspond to E_x, below E_y.

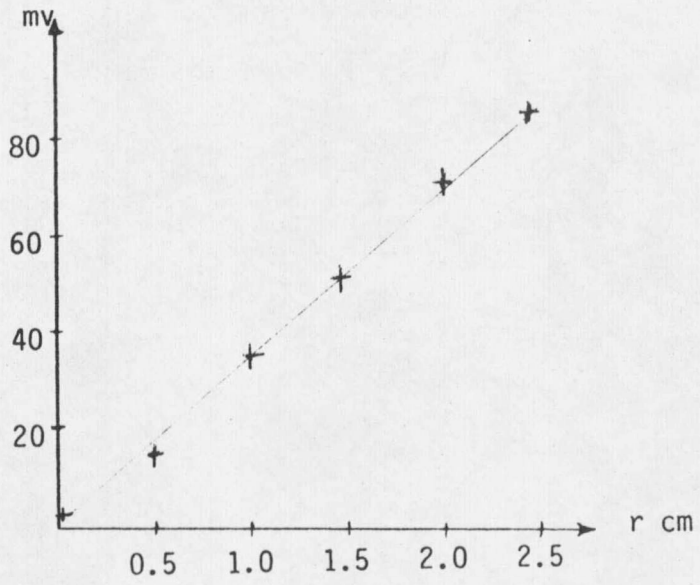


Fig. 29. E_{ϕ} Plot Cylindrical Boundaries.

Table 3 indicates little change was found for E_x (rectangular boundaries) and E_{ϕ} (cylindrical boundaries) versus z for the x,y positions measured. It was assumed that all the x,y positions would show a similar variation with z. This is to say that the field maps of Figures 28 and 29 should have approximately the same relative values at any constant z plane. Because the number of measurements needed to confirm this is enormous, theory describing the variations for the boundary conditions is needed. Although no such theory is considered in this thesis it has been developed by Dr. Bruce R. McLeod [8].

Apparent discrepancies between Figure 28 and Table 3 are explained by noting the following: although the same relative variations in a specific plane were measured from day to day the same magnitudes were not. This is to say that on a given day a position (same x, y and z location) would measure one value and several days later a different value. This could have been due to a polarization effect of the dipole and further research is needed to

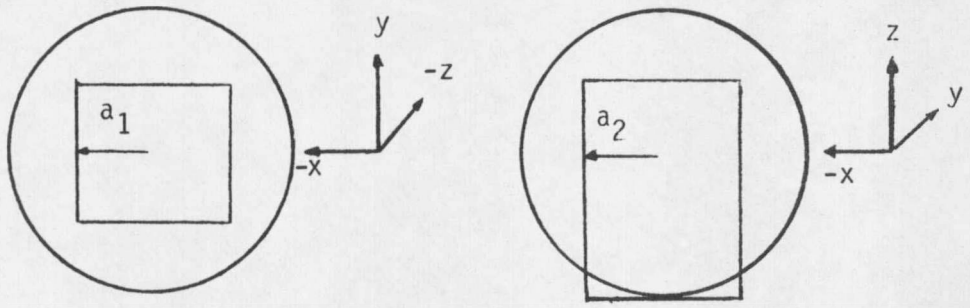
pinpoint the problem; however, the same relative magnitudes were consistently found for a specific plane from day to day.

From Figures 28 and 29 it can be concluded that cells suspended in a solution in a container with horizontal orientation (Fig. 19) would be subjected to non-uniform levels of $\bar{E}$. However, to say that this orientation is not optimum from a constant $\bar{E}$ point of view is a hasty judgment. At least $\bar{E}$ does not vary significantly in the z direction and no z component of $\bar{E}$ exists. An examination of $\bar{E}$-created by the orientation of Figure 20 will show neither of these statements is true.

Vertical Orientation

Figure 31 illustrates the field variations for a rectangular box with the coils vertical at the plane 2.5 in. above the bottom of the box with a 3 in. water level. The points here correspond to those of Figure 22, where as before, the symmetry of the system implies that only the field variations in one quadrant of the box need be known in order to describe the variation of a particular plane. The y components of $\bar{E}$ were not plotted because oscilloscope values relating to them ranged from 2-5 mv and they were assigned insignificant compared to E_x. It is pointed out the component referred to previously as B_z is now B_y due to re-orienting the coils. Since B_y is now the applied magnetic field component there should be no E_y component as the experimental results indicate (assuming no low back EMF). Such a result is expected because $\bar{E}$ and $\bar{B}$ are always at right angles to each other except in the case of dielectric or magnetic tensor material. B_r could give rise to E_y however. Also, this orientation (vertical) requires a z component of $\bar{E}$. This component was not measured directly for the orientation of Figure 20; however, E_z for Figure 20 would show

approximately the same variation found for E_y for the orientation of Figure 19. This idea is best explained through Figure 30.



Horizontal orientation Vertical orientation

Fig. 30. Comparison of E_y and E_z for Horizontal and Vertical Orientations Respectively. Variation of E_y Along a_1 Would Be Similar to the Variation of E_z Along a_2.

Variations for a specific plane in the cylindrical container with vertical orientation are given in Table 4 for the x,y positions of Figure 32. Here again E_y was not significant and E_z was not measured for this specific orientation. The z dimension where the x,y plane was located was the same as for the square box with this orientation. However, the following difference should be noted: in order to keep the boundaries of the container within the coils a new cylindrical boundary was used which was unable to hold 3 in. of water. Here the cylinder was filled with 2.5 in. of water and positioned on styrofoam in order that the measurements could be taken at the same approximate z location as with the rectangular boundary with the coils vertical (Figure 33).

When the cylindrical boundary was filled with 0.5 in. of water the following interesting results was obtained: the plot of x variation exhibited less variation than before and the results are displayed in Table 5. Plus the values were lower by about 2.8. This was to be

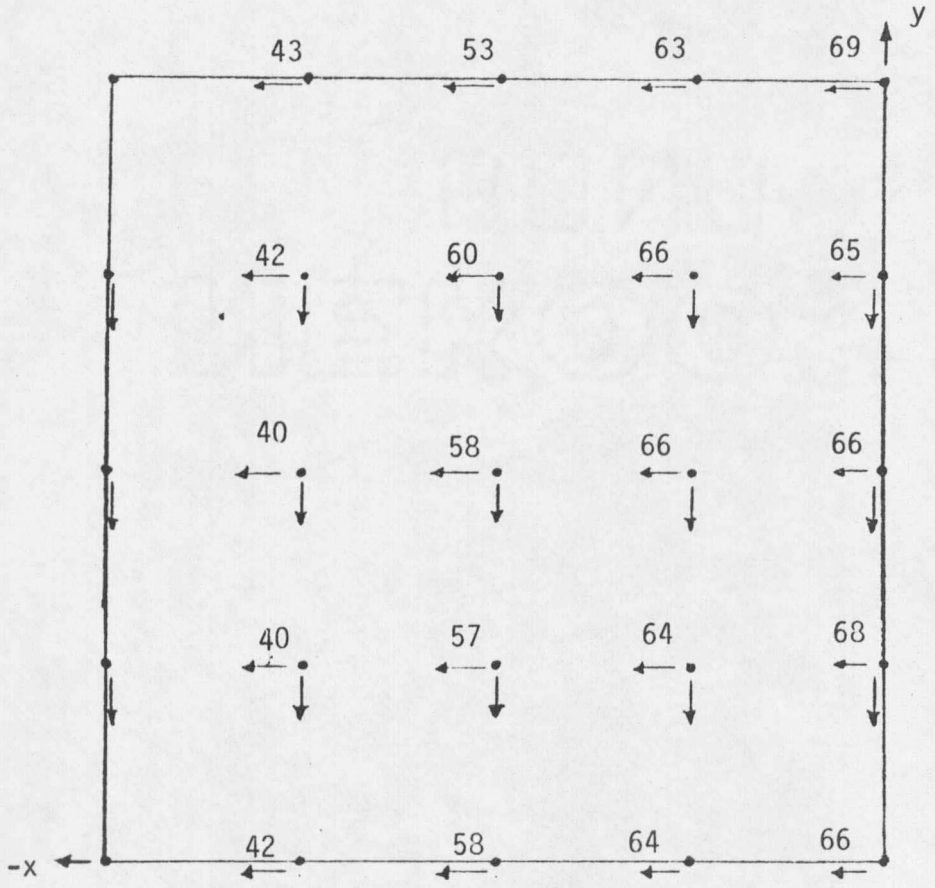


Fig. 31. Plane x,y at z = 2.5 in. Above Bottom of Box. All Values in mvolts.

expected. The values in Table 5 are lower than those of Table 4 because less surface area of water was exposed to the magnetic field to obtain the values of Table 5. Since the fields of Table 5 exhibit less variation than those of Table 4, this suggests the fields become more uniform (with respect to x and y at a particular z plane) as the amount of water in the container is decreased.

Both containers exhibited a marked variation of E_x in the z direction for the orientation of Figure 20. The variation was present regardless of the water level and is described

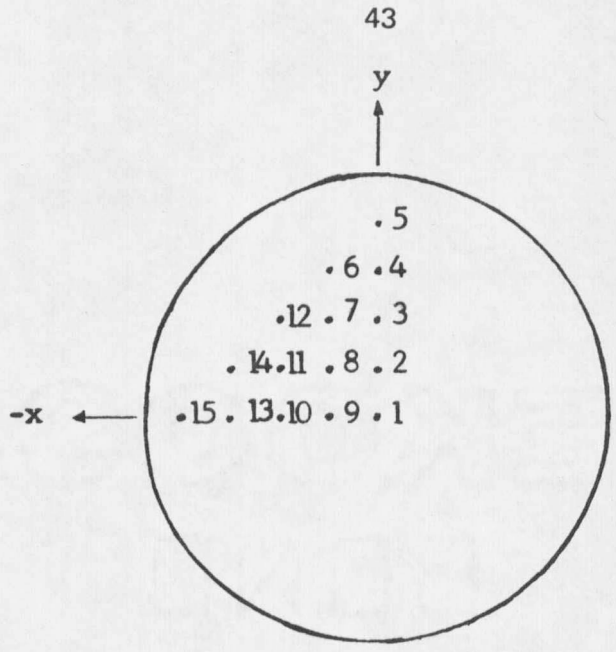


Fig. 32. Positions Coils Vertical.

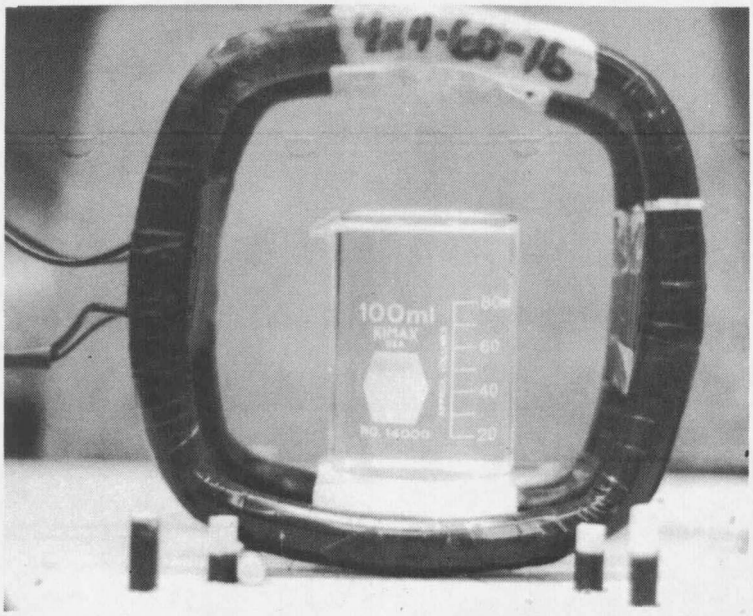


Fig. 33. Relative z Position and Water Level.

Table 4. Relative E_x Values Corresponding to Figure 32 Coils Vertical z Position as Figure 33.

Positions	Values (mv)
1	51
2	49
3	47
4	44
5	40
6	44
7	48
8	47
9	48
10	40
11	39
12	38
13	31
14	31
15	20

Table 5. Relative E_x Values Corresponding to 0.5 in. Water, Coils Vertical.

Positions	Values (mv)
1	17
2	18
3	17
4	18
5	19
6	18
7	18
8	19
9	19
10	18
11	19
12	19
13	19
14	19
15	17

as follows: measurements of E_x starting at the top or bottom of the water level of the container yielded a maximum value which decreased with z until the approximate center of the water was reached where the value of E_x went to zero. Passing through the center point caused the waveform to change polarity and increase again. Equal and opposite values of E_x were found at the top and bottom of the water levels of the containers. This same type of variation was observed for E_x and E_y pertaining to Figure 22. There E_y was observed to go from a maximum value at the edge of the box to zero at the origin and then change sign and go to the same maximum value at the opposite edge of the box. Such variations were observed along constant y and z coordinates. Again, although not confirmed experimentally, E_z for the orientation of Figure 20 would show a variation with x similar to the variation discussed above.

Chapter IV

CONCLUSIONS

Free space variations of the fields found in Chapter I are applicable to horizontal coils with cylindrical boundaries centered between them. These results show that cells at various radial positions will be exposed to markedly different values of E_ϕ. However, the z variation of $\bar{E}$ at a particular radius is quite small. The use of rectangular boundaries with horizontal orientation also causes a wide variation of $\bar{E}$. It would seem that both of these containers would be ineffective in providing a uniform value of $\bar{E}$ throughout a specific plane. However, the horizontal orientation of Figure 20 should guarantee near uniform B_z as long as the dimensions of the container stay within 60 percent of the radius of the coils used.

Results indicate that the vertical orientation *may* provide for the most uniform $\bar{E}$ field throughout a specific plane. However, the E_z component which is present for this orientation will have a marked variation as discussed in the previous chapter. Figure 34 shows that E_z in free space will range from zero to a nonzero value throughout any plane.

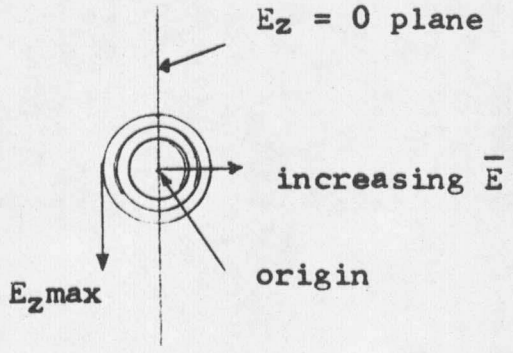


Fig. 34. $\bar{E}$ Lines for Vertical Coils.

Boundaries will alter this free space variation of Figure 34 somewhat. However, there is no reason to believe the vertical orientation would lend itself to more uniform fields than the horizontal orientation if the following condition is examined. If the cells are suspended in free space throughout a particular plane and excited by the coils from both orientations as shown in Figures 35 and 36, of the magnitude of $\bar{E}$ will vary markedly in both cases. This situation could be realized by plating cultures on a nonconducting media and exposing them to the coils at the various orientations. No advantage of one method over the other can be seen if the cells are exposed as in Figures 35 and 36. However, if the dish of Figure 35 were moved closer to one coil, i.e., move the whole plane of cells up or down in the z direction in Figure 35, the variation of E_z would decrease. Now, however, B_z is no longer uniform and B_r will become significant. Thus, the problem of uniform $\bar{E}$ is solved but variations of $\bar{B}$ are greater and neither orientation seems adequate in regards to uniform fields for a plate of cells.

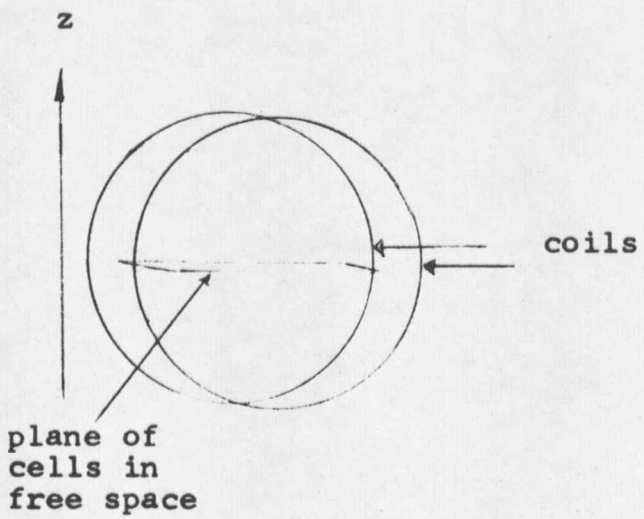


Fig. 35. Vertical Coils.

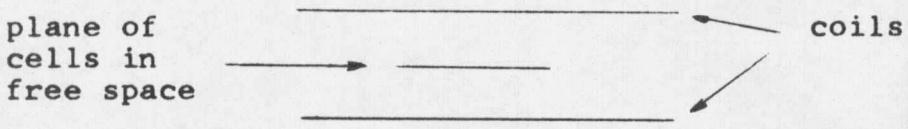


Fig. 36. Horizontal Coils.

Suggested Optimum System

Since the fields for horizontal coils with cylindrical centered containers are the easiest to describe, it seems reasonable to start there in the search of an optimum container from a constant field standpoint. Because tangential $\bar{E}$ components are equal at the boundaries, two coaxial cylinders centered at the origin of the DCS should provide a more uniform field pattern than any setup previously considered. This type of setup is displayed in Figure 37. Of course the DCS must be of horizontal orientation to maintain constant applied magnetic field and uniformity of $\bar{E}$ should improve with decreasing d_1. By keeping the radius of the outer coaxial cylinder within the region of uniform B_z all cells in the suspension should be exposed to nearly the same $\bar{E}$ (and hence current density). Experimental work is needed to confirm the validity of the hypothesis but theory would indicate such an orientation is better than others examined thus far from a constant fields view. This same idea can be extended to cells plated out on a dish. Figure 38 illustrates this concept.

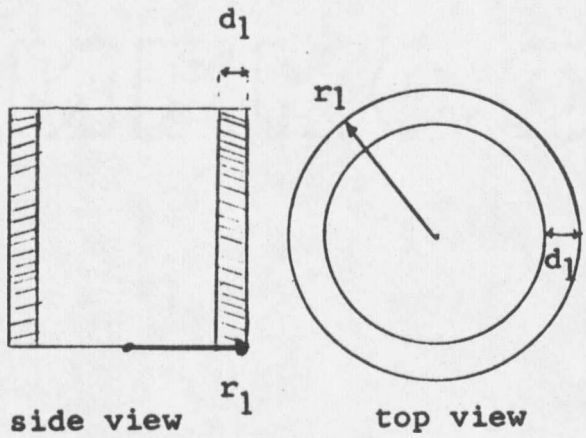


Fig. 37. Proposed Optimum Boundary for Cells in Suspension Crossed Region Area of Ringer's Solution.

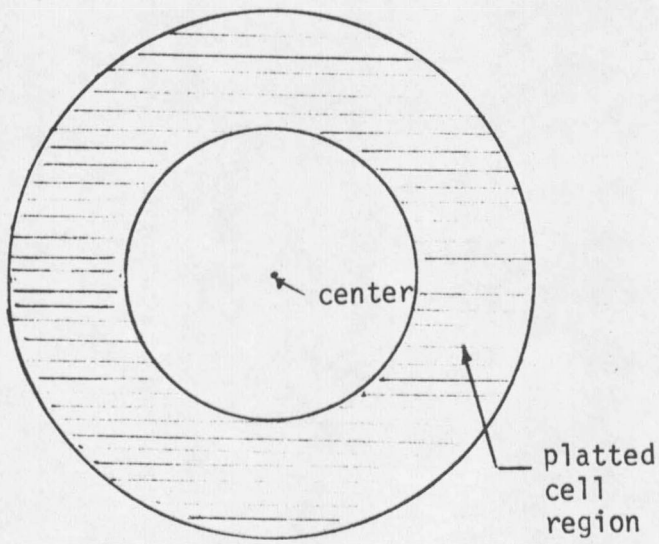


Fig. 38. Proposed Optimum for Cells in a Plated Culture, Crossed Region. Center of Culture Should Be Centered at Center of DCS in the Horizontal Orientation.

BIBLIOGRAPHY

BIBLIOGRAPHY

1. Bassett, C. A. L., and Becker, R. O., "Generation of Electric Potentials in Bone Response to Mechanical Stress," *Science* 137:1063, 1962.

2. Adey, W. R., "Frequency and Power Windowing in Tissue Interactions with Weak Electromagnetic Fields," *Proc. of IEEE*, 68, No. 1, Jan. 1980, pp. 119-125.

3. Smith, S. D., and Pilla, A. A., "Modulation of Newt Limb Regeneration by Electromagnetically Induced Low Level Pulsating Current," In Press: *Mechanisms of Growth Control*, Ed. R. Becker, C. C. Thomas Press, New York, 1981.

4. Pilla, A. A., Bioelectrochemistry Laboratory, Orthopedic Research, Departments of Chemical Engineering and Applied Chemistry and Orthopedic Surgery, Columbia University, New York, New York, "The Rate Modulation of Cell and Tissue Function Via Electrochemical Information Transfer."

5. Christel, P., Cerf, G., and Pilla, A. A., "Modulation of Rat Radial Osteotomy Repair Using Electromagnetic Current Induction," *Mechanisms of Growth Control*, Ed. R. Becker, C. C. Thomas Press, New York, 1981.

6. Pilla, A. A., Seminar at Montana State University, June 9, 1981.

7. Gandhi, P., "State of the Knowledge of EM Absorbed Dose in Man," *Proceedings IEEE Special Issue Biological Effects and Medical Applications*, January 1980.

8. McLeod, B. R., Pilla, A. A., and Sampsel, M. W., "Electromagnetic Fields Induced by Helmholtz Aiding Coils Inside Saline Filled Boundaries," In Preparation.

9. Smythe, W. R., *Static and Dynamic Electricity*, McGraw-Hill Book Company, 1950, p. 271.

10. Straton, J. A., *Electromagnetic Theory*, McGraw Hill Book Company, 1941, p. 263.

11. Vaughan, J. R., "Axisymmetric Magnetic Fields in Computer Programs," *IEEE Electron Devices*, February 1972, pp. 141-151.

12. Halliday, D., and Resnick, R., *Physics*, John Wiley and Sons, Inc., 1966, p. 869.

13. McLeod, B. R., Montana State University, private communication.

14. Brown, G. H., Hoyler, C. N., and Bierworth, R. A., *Radio Frequency Heating*, D. Van Nostrand Company, Inc., 1947, pp. 27-30.

15. Spiegel, M. R., Schaum's Outline of Theory and Problems of Probability and Statistics, 1975, p. 161.

16. Spiegel, M. R., Schaum's Outline of Theory and Problems of Probability and Statistics, 1975, p. 262.

APPENDICES

APPENDIX A

FIELDS PROGRAM

APPENDIX A

FIELDS PROGRAM

```
      ************************************************************
      ************              FIELDS                ************
      *                                                          *
      *      PROGRAM FINDS AO BZ BR AO*BZ FOR A=THE              *
      *         FIXED RADIUS OF THE COILS Z1 IS THE FIXED        *
      *       DISTANCE BETWEEN THEM AND ZP IS THE DISTANCE       *
      *         ABOVE THE Z=Ø.Ø PLANE                            *
      ************************************************************
ØØØ1          REAL*8 R,Z,AM,AK,E,AO,BR,BZ,A,Z1,ZP
      C       CREATE SCALE VALUES CONTINGENT ON COIL CURRENT AND
      C       ITS TIME DERIVATIVE
ØØØ2          PI = 3.141529
ØØØ3          ASCALE = 137.E-Ø3
ØØØ4          BSCALE = 14.4E-Ø6
ØØØ5          HSCALE = 1/(PI*4E-Ø7)
ØØØ6          WRITE(22,99) ASCALE,BSCALE,HSCALE,PI
ØØØ7    99    FORMAT(4E13.4)
      C       INITIALIZE VALUE OF RADIUS
ØØØ8          R = Ø.ØØØØØØØ1Ø
      C       COMPUTE 41 VALUES OF B & A
      C       Z1=DISTANCE BETWEEN COILS,A=RADIUS,ZP=Z PLANE
      C       READ VALUES IN IN METERS
ØØØ9          READ(3,1ØØ)Z1,A,ZP
ØØ1Ø    1ØØ   FORMAT(3F12.8)
      C       SET UP CHANGE IN RADIUS VALUE
ØØ11          DR=A/4Ø.Ø
ØØ12          DO 4Ø I=1,41
      C       SET UP FLAG TO CHANGE Z COORDINATE
ØØ13          F=Ø.Ø
      C       SET Z COORDINATE FOR ONE COIL
ØØ14          Z=Z1/2.Ø+ZP
      C       CHANGE VALUE OF Z FOR 2ND COIL IF FIRST VALUE FOUND
ØØ15    1Ø    IF(F.EQ.1.Ø)Z=ZP-Z1/2
      C       AM=K**2 (SEE STRATON PAGE 263)
ØØ16    11    AM=4*R*A/((A+R)**2+Z*Z)
ØØ17          CALL ELLIPTIC(AK,E,AM)
      C       COMP. HAVE BEEN NORMALIZED BY UI/2PI; HOWEVER THE
      C       SCALE FACTORS MAKE THEM CORRECT.
      C       COMP PHEE OF THE VECTOR MAG POTENTIAL
ØØ18          AO=2*SQRT(A/(R*AM))*((1-AM/2)*AK-E)
      C       PARAMS. FOR MAG. FIELD DENSITY CALC.
ØØ19          AN=SQRT((A+R)**2+Z*Z)
ØØ2Ø          C=(A-R)**2+Z*Z
ØØ21          BR=(Z/(R*AN))*(-AK+(A*A+R*R+Z*Z)*E/C)
ØØ22          BZ=(AK+(A*A-R*R-Z*Z)*E/C)/AN
ØØ23          IF(F.EQ.1.Ø) GO TO 2Ø
      C       SAVE VALUES OF FIELD DUE TO ONE COIL
ØØ24          AO1=AO*ASCALE
ØØ25          BR1=BR*BSCALE
ØØ26          BZ1=BZ*BSCALE
ØØ27          F=1.Ø
ØØ28          GO TO 1Ø
      C       USE SUPERPOSITIN FIND FIELDS AT PARTICULAR R & Z
ØØ29    2Ø    AO=AO1+AO*ASCALE
ØØ3Ø          BR=BR1+BR*BSCALE
ØØ31          BZ=BZ1+BZ*BSCALE
ØØ32          AB=AO*BZ*HSCALE
```

```
      C       ELLIPTIC SUB. EVALUATES ELLIPTIC INTEGRALS
ØØØ1          SUBROUTINE ELLIPTIC'BK,BE,BM)
ØØØ2          REAL*8 BK,BE,BM
ØØØ3          IF(BM.LT.Ø.Ø)GO TO 6Ø
ØØØ4          IF(BM.GT..999) GO TO 6Ø
ØØØ5          Q6=1.Ø
ØØØ6          Q5=Q6
ØØØ7          Q7=SQRT(1.Ø-BM)
ØØØ8          Q9=BM
ØØØ9    2Ø    Q8=Ø.5*(Q5-Q7)
ØØ1Ø          Q5=Ø.5*(Q5+Q7)
ØØ11          Q7=SQRT(Q7*(Q5+Q8))
ØØ12          Q6=2*Q6
ØØ13          Q9=Q9+Q6*Q8*Q8
ØØ14          IF(Q8.GT.Ø.1E-Ø5)GO TO 2Ø
ØØ15          BK=Ø.5*3.14159265/Q5
ØØ16          BE=BK*(1.Ø-Ø.5*Q9)
ØØ17          RETURN
ØØ18    6Ø    WRITE(1Ø8,5Ø)BM
ØØ19    5Ø    FORMAT('M ENTERED IN ERROR M ='F8.4)
ØØ2Ø          STOP
ØØ21          END
```

APPENDIX B

FOURIER PROGRAM

APPENDIX B

FOURIER PROGRAM

```
      ************************************************************
      *                    FOURIER                               *
      *                                                          *
      *          PROGRAM FINDS FOURIER SERIES                    *
      *               OF WAVEFORM WITH 5MSEC BURST               *
      ************************************************************
0001            IMPLICIT DOUBLE PRECISION (A-H,O-Z)
0002            DIMENSION A(10000),B(10000),FT(10000)
0003            INTEGER F
0004            READ(20,*) TOWEL1,TOWEL2,TOWEL3,TOWEL4,F,NCOMP
0005            WRITE(10,10)TOWEL1,TOWEL2,TOWEL3,TOWEL4,F,NCOMP
0006      10    FORMAT(4(2X,E12.6),2X,I2,2X,I7)
          C     SET UP EQUAL AREA FACTOR
0007            G = TOWEL1/TOWEL2
0008            G = TOWEL1/TOWEL2
0009            H = (G+1.0)
          C     CREATE AN INTEGER NUMBER OF INTEGRATIONS
          C     PER BURST
0010            NPULS = INT(TOWEL4/(TOWEL1+TOWEL2+TOWEL3))
0011            TOW12 = TOWEL1 + TOWEL2
0012            TOW123 = TOW12 + TOWEL3
0013            PI = 3.1415926
0014            W = 2*PI*F
          C     SET INITIAL INTEGRATION LIMITS
0015            DO 40 N=1,NCOMP
0016            RLOLIM = TOWEL1
0017            UPLIM = TOW12
0018            ROLIM = TOW123
0019            C = N*PI
          C     INTEGRATE ONE PERIOD OF WAVEFORM
0020            DO 30 I=1,NPULS
          C     SET CONSTANTS
          C     SIN & COS ARGUEMENTS
0021            EE = W*N*RLOLIM
0022            FF = W*N*UPLIM
0023            HH = W*N*ROLIM
0024            IF(I.NE.1)GO TO 55
0025            ASAVE = (H*SIN(EE)-G*SIN(FF))/C
0026            BSAVE=(G*COS(FF)-H*COS(EE))/C
0027            GO TO 66
0028      55    ASAVE=(H*SIN(EE)-G*SIN(FF)-SIN(HH))/C
0029            BSAVE=(G*COS(FF)-H*COS(EE)+COS(HH))/C
0030            ROLIM = ROLIM + TOW123
0031      66    A(N)=A(N)+ASAVE
0032            B(N)=B(N)+BSAVE
          C     CHANGE LIMITS OF INT.
0033            UPLIM = UPLIM + TOW123
0034      30    RLOLIM =      RLOLIM+TOW123
          C     ADD COS(0)/C FOR 1ST PULSE ONLY AND ALL N
0035      40    B(N)=1.0/C+B(N)
0036            WRITE(7)A,B
0037            END
```

APPENDIX C

TIME PROGRAM

APPENDIX C

TIME PROGRAM

```
      ************************************************************
      *          TIME FUNCTION FROM FOURIER                      *
      *               PROGRAM FINDS F(T)                         *
      *            GIVEN THE COMP. FROM DISK                     *
      ************************************************************
0001            IMPLICIT DOUBLE PRECISION (A-H,O-Z)
0002            DIMENSION A(10000),B(10000),FT(200)
0003            DPI=3.141592654
0004            DW=40*DPI
0005            TCHNG=1.30E-06
0006            READ (7)A,B
0007            T=200.0E-06
0008            DO 70 I=1,200
0009            FT(I)=0.0
0010            DO 60 J=1,10000
0011            FF=DW*J*T
0012            FSAVE=A(J)*COS(FF)+B(J)*SIN(FF)
0013      60    FT(I)=FT(I)+FSAVE
0014            WRITE(13,18)T,FT(I)
0015            T=T+TCHNG
0016      18    FORMAT(2E12.6)
0017      70    CONTINUE
0018            END
```

APPENDIX D

MUTUAL INDUCTANCE, INDUCTANCE, COEFFICIENT OF COUPLING CURRENT AND CURRENT DERIVATIVE DETERMINATIONS

APPENDIX D

MUTUAL INDUCTANCE, INDUCTANCE, COEFFICIENT OF COUPLING CURRENT AND CURRENT DERIVATIVE DETERMINATIONS

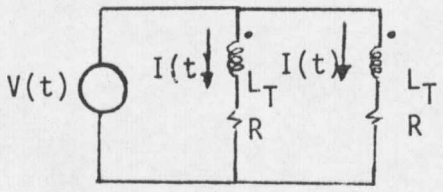


Fig. 39. DCS Schematic.

The coils of the DCS were taken off the driver and connected to an inductance bridge at terminals a and b for both orientations in Figures 40 and 41. The formulas which follow were used to find M, the mutual inductance.

$$L_1 + L_2 + 2M = 1.97 \text{ mHenerys (measured via Fig. 41)}$$

$$L_1 + L_2 - 2M = 1.42 \text{ mHenerys (measured via Fig. 40).}$$

Where: $L_1 = L_2 = 850$ microHenerys. And M was found to be 132 microHenerys. Thus, $L_T = 980$ microHenerys, i.e., $L_1 + M$. Also, $M = k_c \sqrt{L_1 L_2}$ and $k_c = 0.15$; where k_c is the coefficient of coupling.

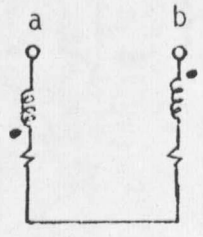


Fig. 40. Circuit to Find M.

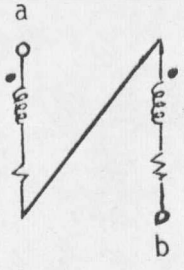


Fig. 41. Circuit to Find M.

EQUATION TO FIND I(t) AND $\partial I(t)/\partial t$.

$$V(t) = L_T \partial I(t)/\partial t + RI(t)$$

Trying a solution for I(t) yields $I(t) = Dte^{-300t}$. Where $V(t) = 12e^{-300t}$ (see Figures 42 and 43). Where 300 is the time constant of the exponential decay of V(t) for the positive portion of the pulse. Differentiating yields:

$$\partial I(t)/\partial t = D[e^{-300t} - 300te^{-300t}]$$

Thus $D = 12/L_T$ since $V(t) = 12e^{-300t}$. Finally:

$$\partial I(t)/\partial t \ (t = 0.1 \text{ msec}) = 11{,}500 \text{ amperes/sec.}$$

$$I(t) \quad (t = 0.1 \text{ msec}) = 1.18 \text{ amperes.}$$

Where the preceding two equations were used as scaling factors in the theoetical equations for E_ϕ and B_z respectively.

APPENDIX E

V(t) FOR DIFFERENT ITS's AND I(t) FIGURES

APPENDIX E

V(t) FOR DIFFERENT ITS's AND I(t) FIGURES

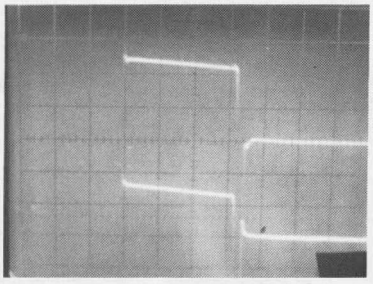


Fig. 42. V(t) (upper trace) Induced Waveform for L_{ITS} of 2.0 microHenerys (lower trace). Horizontal scale 0.1 msec/div, vertical scale upper trace 5 v/div lower trace 10 mv/div.

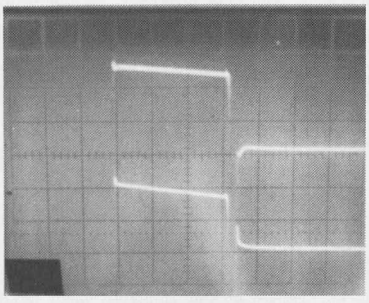


Fig. 43. V(t) (upper trace) Induced Waveform for L_{ITS} of 4.0 microHenerys (lower trace). Horizontal scale 0.1 msec/div, vertical scale upper trace 5 v/div lower trace 50 mv/div.

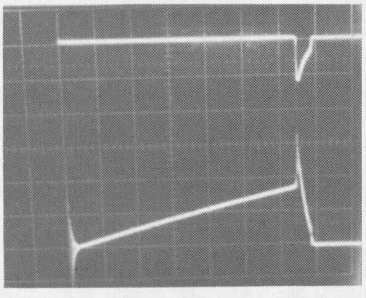


Fig. 44. I(t) (lower trace) An Induced Waveform (upper trace). Horizontal scale 50 microsec/div, vertical scale 2 amps/div lower trace, 5 v/div upper trace.

APPENDIX F

METHOD TO CALCULATE B_z FROM EXPERIMENTAL MEASUREMENTS

APPENDIX F

METHOD TO CALCULATE B_z FROM EXPERIMENTAL MEASUREMENTS

Since $\overline{ds}$ is stationary

$$EMF = - \partial/\partial t \int \bar{B} \cdot \overline{ds}$$

Assuming B_z is approximately constant with respect to $\overline{ds}$

$$16\Delta s \int_{B_z(0)}^{B_z(t_1)} \partial B_z = - \int_0^{t_1} EMF\, \partial t$$

where Δs is the surface area of the B_z ITS and 16 is included because the ITS consisted of 16 turns.

For an EMF at r = 0.01 m and z = 0 it follows that

$$16\Delta s \int_{B_z(0)}^{B_z(t_1)} B_z = \int_0^{t_1} 11e^{-400t}\, \partial t; \text{ the EMF is in mvolts}$$

Since $B_z(0)$, i.e., B_z at time zero, is zero assuming no current then,

$$B_z(t_1) = \frac{-11}{400\,(16)\,\Delta s}\,[1 - e^{-400t_1}]$$

With $\Delta s = 68\ mm^2$ and $t_1 = 0.1$ msec it follows that

$$B_z(t_1) = -0.99\ mW/m^2$$

The theoretical value of B_z for the same radius and time is $-0.99\ mW/m^2$.

APPENDIX G

TIME OUTPUT

APPENDIX G

TIME OUTPUT

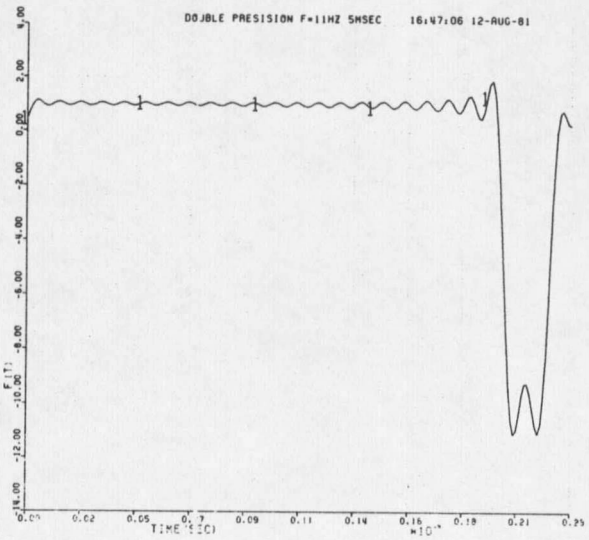


Fig. 45. Time Output of 11 Hz Repetition Rate Burst Waveform. Ten thousand components computed in FOURIER were used in TIME to obtain Figure 45.

APPENDIX H

FACTORS USED TO FIND THE VOLTAGE SPECTRUM OF FIGURE 13

APPENDIX H

FACTORS USED TO FIND THE VOLTAGE SPECTRUM OF FIGURE 13

Real part:

$$\frac{A}{a^2+\omega^2}\left[a - e^{-a\tau_1}\left(a\cos(\omega\tau_1) - \omega\sin(\omega\tau_1)\right)\right] +$$

$$\frac{|B|}{b^2+\omega^2}\left[e^{-b\tau_2}\left(b\cos(\omega\tau_3) - \omega\sin(\omega\tau_3)\right) - \left(b\cos(\omega\tau_1) - \omega\sin(\omega\tau_1)\right)\right]$$

Imaginary part:

$$\frac{A}{a^2+\omega^2}\left[e^{-a\tau_1}\left(\omega\cos(\omega\tau_1) + a\sin(\omega\tau_1)\right) - \omega\right] +$$

$$\frac{|B|}{b^2+\omega^2}\left[\left(\omega\cos(\omega\tau_1) + b\sin(\omega\tau_1)\right) - e^{-b\tau_2}\left(\omega\cos(\omega\tau_3) + b\sin(\omega\tau_3)\right)\right]$$

The square root of the sum of the squares of the real and imaginary parts were then plotted versus frequency in Figure 13. If power densities are desired the magnitudes of Figure 13 must be squared. Also, the value at one megaHz is down 40 dB from the value at 2 kHz.

Parameter values used were:

$A = 10^6$; $|B| = 23A$; $a = 420$; $b = 58{,}000$; $\tau_1 = 320$ microsec; $\tau_2 = 20$ microsec; $\tau_3 = 340$ microsec; $\omega = 2\pi f$.

The real and imaginary parts were determined by performing the Fourier transform integral on the waveform of Figure 46.

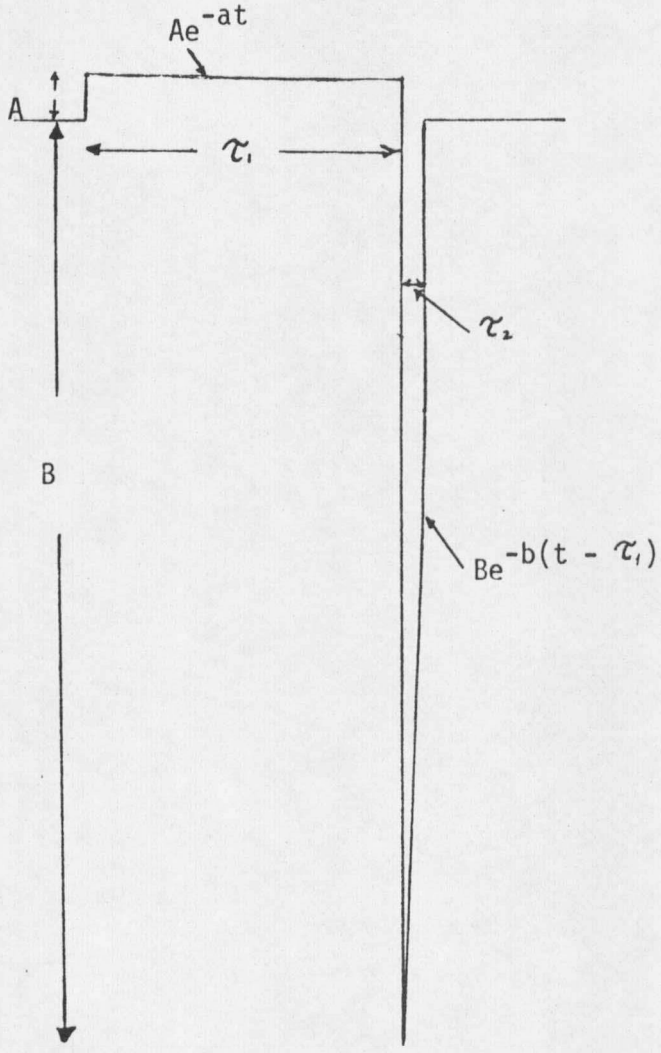


Fig. 46. Waveform Used to Compute Real and Imaginary Parts on Preceding Page. Where $\tau_3 = \tau_1 + \tau_2$.

APPENDIX I

PROOF OF EQUAL ENERGY AND EQUAL AREA OF THE SQUARE WAVE APPROXIMATION

APPENDIX I

PROOF OF EQUAL ENERGY AND EQUAL AREA OF THE SQUARE WAVE APPROXIMATION

Assume: Coil used to measure the induced voltage is a pure inductor.

Therefore, $Vdt = Ldi$

The variables which follow refer to Figure 47.

Assume when $t = 0; i = 0$

Then $V_{1m}dt = Ldi$; $V_{1m}t_1 = Li_1$

$V_{2m}dt = Ldi$; $-V_{2m}(t_2 - t_1) = L(i_2 - i_1)$

and assuming $i_2 = 0$ yields

$V_{1m}t_1 = V_{2m}(t_2 - t_1)$; which shows equal area in the two pulses.

For equal energy,

$i(t) = I_m t/t_1$; $i_1(t) = -I_m t/(t_2 - t_1) + b$; $b = I_m t_2/(t_2 - t_1)$

Therefore, the energy in the positive pulse E_1 is found from the following equation.

$E_1 = (V_{1m}I_m t/t_1)dt$; which equals $V_{1m}I_m t_1/2$

Now the energy in the negative pulse

$E_2 = V_{2m}(-I_m t/(t_2 - t_1) + I_m t_2/(t_2 - t_1))dt.$

Performing the integration yields

$E_2 = (V_{2m}I_m/(t_2 - t_1))(t_2^2/2 + t_1^2/2 - t_2 t_1)$;

where the last factor factors to $(t_2 - t_1)^2/2$.

Therefore, because of the equal area criterion already established; i.e., $V_{1m}t_1 = V_{2m}(t_2 - t_1)$, the pulses have equal energy as well.

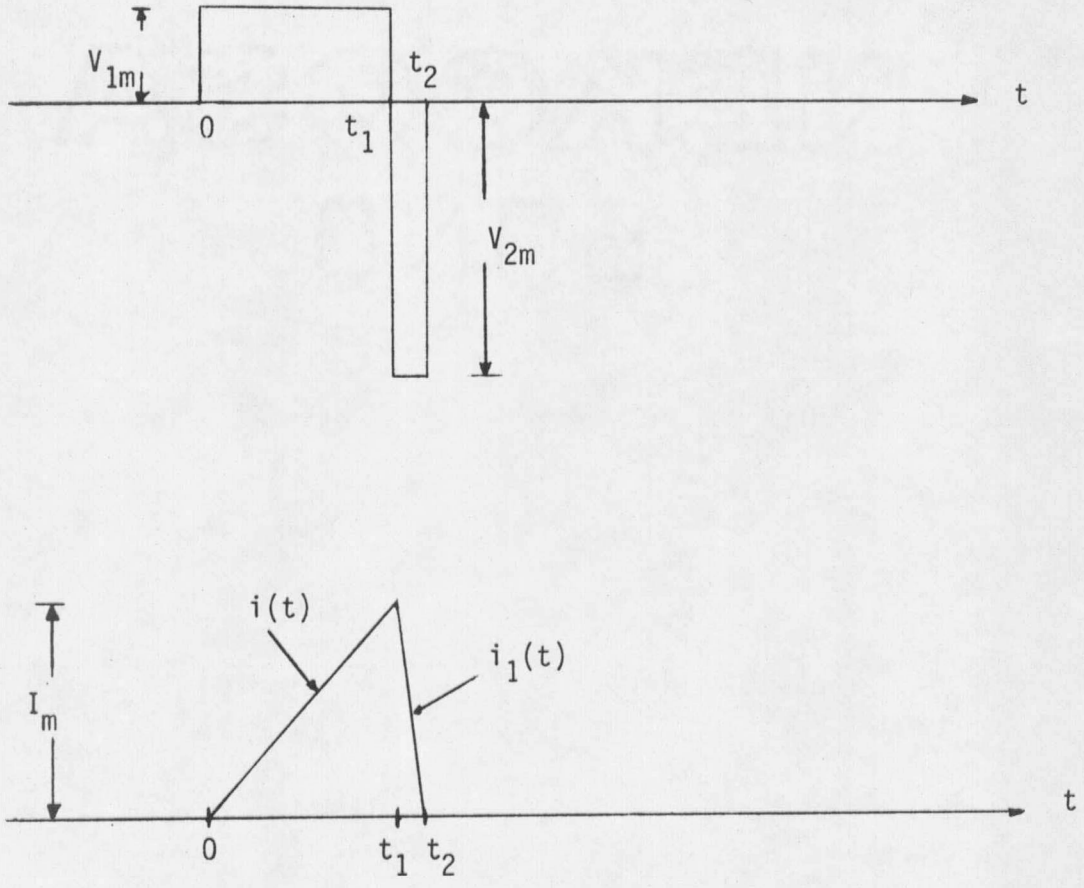


Fig. 47. Voltage and Current Waveforms for Equal Energy Calculations.

APPENDIX J

"STUDENT'S" t TEST

APPENDIX J

"STUDENT'S" t TEST

The statistic t was generated using the following formula [15]:

$$t = \frac{\bar{X} - u}{S/\sqrt{n-1}}$$

Where $\bar{X}$ is the average of the E_x's or E_y's of Table 6, i.e., the values plotted in Figure 28; u is a proposed mean value; n is the number of samples (four in this case); S was computed as follows:

$$S^2 = \frac{(X_1 - \bar{X})^2 + (X_2 - \bar{X})^2 + \cdots + (X_n - \bar{X})^2}{n}$$

Here X_1 are the values of E_x or E_y for t_x or t_y respectively in Table 6.

The value of u was chosen to be $\bar{X} + \bar{X}(0.1)$. In doing so the test will show the probability of the hypothetical mean (u) being 10 percent larger than the measured mean. Calculated values of t for the preceding conditions are displayed in Table 6.

Since $t_{.95}$ is -2.13 for the values of Table 6 it can be seen that the hypothesis is significant for some of the points at the 0.05 level, i.e., we can be 95 percent sure the actual mean of the point is not 10 percent higher than the measured mean. This idea is valid for points with t less than -2.13. If the factor of 0.10 is changed to 0.20 so we are now testing the hypothesis that the mean value is 20 percent greater than the measured mean all but seven values of t are less than -2.13. Thus, approximately 85 percent of the time we can be 90 percent confident that the measured mean values were within 20 percent of the actual mean values.

Table 6. Measured Values of E_x and E_y and Corresponding t Values.

	E_x	E_y	E_x	E_y	E_x	E_y	E_x	E_y	t_x	t_y
1.	3	3	3	3	2	2	3	3	-1.1	-1.1
2.	3	14	6	13	2	12	3	12	-0.404	-2.66
3.	0	32	3	28	2	30	2	36	-.28	-1.8
4.	3	44	4	48	3	48	3	54	-1.3	-2.4
5.	-	80	-	75	-	76	-	80	-	-5.9
6.	-	76	-	70	-	76	-	80	-	-3.7
7.	10	44	7	44	4	48	5	56	-0.5	-1.7
8.	14	28	13	26	9	28	10	34	-0.97	-1.7
9.	12	14	12	12	12	14	12	14	infinite	-2.7
10.	14	3	12	2	12	2	14	2	-2.3	-0.9
11.	-	68	-	60	-	64	-	76	-	-2.0
12.	14	44	15	40	12	40	10	48	-1.2	-2.2
13.	24	20	22	26	21	22	20	30	-2.5	-1.1
14.	24	10	26	12	26	12	27	14	-4.1	-1.5
15.	35	3	26	2	27	3	29	2	-1.4	-0.9
16.	47	3	44	3	44	1	49	2	-3.8	-0.5
17.	44	6	40	12	44	7	48	10	-2.7	-0.6
18.	32	16	38	20	34	14	36	24	-2.7	-0.8
19.	22	24	26	22	20	26	25	33	-1.7	-1.1
20.	-	42	-	40	-	44	-	54	-	-1.4
21.	26	-	24	-	17	-	28	-	-1.0	-
22.	40	-	45	-	46	-	48	-	-2.6	-
23.	64	-	60	-	60	-	68	-	-3.3	-
24.	72	-	68	-	72	-	80	-	-2.6	-
25.	76	-	76	-	76	-	84	-	-3.9	-

The columns are values of E_x and E_y respectively measured for positions 1-25 of Figure 22. Values not shown could not be measured due to size of the dipole.

APPENDIX K

STANDARD ERROR OF ESTIMATE

APPENDIX K

STANDARD ERROR OF ESTIMATE

The following equation was used to compare the plots of Figures 6-9.

$$S_{y,r} = [\Sigma \frac{(y - y_{est})^2}{n}] \quad (16)$$

Where y_{est} represents the experimental values of E_ϕ or B_z and y represents the theoretical values of E_ϕ and B_z; n is the number of points compared.

Theoretical and experimental values of E_ϕ and B_z used to determine the standard error estimates are displayed in Table 7.

Table 7. Values Used in Standard Error Estimates.

E_ϕ (v/m)			B_z (mw/m^2)		
y	r	y_{est}	y	r	y_{est}
0.06	0.10	0.50	1.02	0.01	0.99
0.08	0.17	0.08	1.02	0.07	0.99
0.11	0.23	0.11	0.98	0.32	0.93
0.12	0.25	0.12	0.97	0.35	0.86
0.15	0.32	0.16	0.78	0.50	0.72
0.17	0.36	0.17	0.44	0.64	0.32
0.18	0.38	0.19			
0.20	0.43	0.21			
0.20	0.46	0.21			
0.24	0.58	0.23			
0.05	0.10	0.05	1.02	0.15	0.99
0.09	0.17	0.08	1.07	0.25	1.02
0.11	0.23	0.11	1.09	0.36	1.07
0.12	0.25	0.12	1.15	0.43	1.11
0.15	0.32	0.16	1.19	0.51	1.16
0.18	0.36	0.17	1.18	0.53	1.13
0.19	0.38	0.20			
0.23	0.43	0.22			

Where units of r are meters $\times 10^{-1}$.

$S_{y,r}$ and the average values of y are shown in Table 8.

Table 8. RMS Value of Difference and Measured Average Values.

	$S_{y,r}$	$\bar{y}$
E_ϕ (v/m)	0.008	0.15
B_z (mw/m^2)	0.000076	0.87
E_ϕ (v/m)	0.008	0.14
B_z (mw/m^2)	0.000038	1.11

APPENDIX L

DEFINITIONS OF VARIABLES AND OPERATIONS

APPENDIX L

DEFINITIONS OF VARIABLES AND OPERATIONS

$\bar{A}$	Magnetic vector potential
$\bar{D}$	Electric flux density vector
$\bar{E}$	Electric field intensity vector
$\bar{H}$	Magnetic field intensity vector
$\bar{B}$	Magnetic field density vector
u	Permeability constant, $\bar{B} = u\bar{H}$
ϵ	Permittivity constant, $\bar{D} = \epsilon\bar{E}$
E_i	Component of the general vector, $\bar{E}$, in the i direction
K	Elliptic integrals of the first kind
E	Elliptic integrals of the second kind
ρ	Free charge volume density
$\bar{a}\phi$	Unit vector in the ϕ direction
$\partial I/\partial t$	Partial derivative of I with respect to time
$\nabla \cdot \bar{A}$	Divergence of $\bar{A}$
$\nabla \times \bar{A}$	Curl of $\bar{A}$
$\bar{J}$	Current density vector
σ	Conductivity constant, $\bar{J} = \sigma\bar{E}$
V	Electric scalar potential
∇V	Gradient of V
ϵ_o	Permittivity of free space
ϵ_r	Relative permittivity, $\epsilon = \epsilon_o\epsilon_r$

Φ Magnetic flux

ϕ Direction in cylindrical coordinates

MONTANA STATE UNIVERSITY LIBRARIES
stks N378.Sa47@Theses RL
Experimental investigation of electromag
3 1762 00118766 3

MAIN LIB.
N378
Sa47
cop.2

Sampsel, M. W.
Experimental investigation of electromagnetic fields...

DATE	ISSUED TO

N378
Sa47
Cop 2